Structure and dynamics of the chromatin remodeler ALC1 bound to a PARylated nucleosome

Luka Bacic[1,4], Guillaume Gaullier[1,4], Anton Sabantsev[1], Laura C. Lehmann[1], Klaus Brackmann[1], Despoina Dimakou[1], Mario Halic[2], Graeme Hewitt[3], Simon J. Boulton[3], and Sebastian Deindl[1,5,*]

[1]Department of Cell and Molecular Biology, Science for Life Laboratory, Uppsala University, 75124 Uppsala, Sweden.

[2]Department of Structural Biology, St Jude Children's Research Hospital, Memphis, TN, USA.

[3]The Francis Crick Institute, 1 Midland Road, London NW1 1AT, UK.

[4]These authors contributed equally

[5]Lead Contact

[*]Correspondence: sebastian.deindl@icm.uu.se (S.D.)

ABSTRACT

The chromatin remodeler ALC1 is recruited to and activated by DNA damage-induced poly(ADP-ribose) (PAR) chains deposited by PARP1/PARP2/HPF1 upon detection of DNA lesions. ALC1 has emerged as a candidate drug target for cancer therapy as its loss confers synthetic lethality in homologous recombination-deficient cells. However, structure-based drug design and molecular analysis of ALC1 have been hindered by the requirement for PARylation and the highly heterogeneous nature of this post-translational modification. Here, we reconstituted an ALC1 and PARylated nucleosome complex modified *in vitro* using PARP2 and HPF1. This complex was amenable to cryo-EM structure determination without cross-linking, which enabled visualization of several intermediate states of ALC1 from the recognition of the PARylated nucleosome to the tight binding and activation of the remodeler. Functional biochemical assays with PARylated nucleosomes highlight the importance of nucleosomal epitopes for productive remodeling and reveal that ALC1 preferentially slides nucleosomes away from DNA breaks.

(Words: 147)

INTRODUCTION

DNA double-strand breaks (DSB) are among the most cytotoxic DNA lesions, and a common strategy in cancer therapy is to overwhelm the repair capacity of cancer cells with excess DSBs using radiation or cytotoxic chemotherapies. DSBs can only be repaired successfully if they are first recognized, and their recognition elicits a DNA damage signaling cascade. One of the earliest components of the DNA damage response (DDR) able to recognize DSBs is poly(ADP-ribose) polymerase 1 (PARP1) (Krishnakumar and Kraus, 2010; C. Liu et al., 2017). Targeted inhibition of the DNA damage response in cancer cells is often used alone or in combination to augment the cytotoxic effect of DSBs, as exemplified by clinical PARP inhibitors.

Chromatin remodeling by ALC1 (Amplified in Liver Cancer 1) plays an important role during the early stages of the DDR elicited by poly-ADP-ribosylation (PARylation) at DNA lesions (Sellou et al., 2016). ALC1 uses its macro domain to bind to PAR (Ahel et al., 2009; Gottschalk et al., 2009) produced by PAR polymerases 1 and 2 (PARP1 and PARP2). In the absence of DNA damage, the macro domain of ALC1 is abutted against its ATPase, which stabilizes an inactive conformation (Lehmann et al., 2017; Singh et al., 2017). PAR binding to the macro domain relieves this auto-inhibition upon recruitment to DNA damage (Lehmann et al., 2017; Singh et al., 2017). Full activation of ALC1 requires its linker to insert an Arg anchor motif into the “acidic patch” (AP) composed of negatively charged residues from histones H2A and H2B on both faces of the nucleosome (Lehmann et al., 2020). A PARylation response leading to efficient repair requires HPF1 (histone PARylation factor 1), since cells lacking HPF1 display much-reduced survival after DNA damage (Bonfiglio et al., 2017). As a crucial step in the DNA damage response, activation of ALC1 therefore most likely requires nucleosomal histone PARylation in the presence of HPF1.

Recent studies have defined ALC1 as an attractive target for therapeutic intervention strategies in cancer as its inactivation sensitizes to clinical PARP inhibitors and confers synthetic lethality in homologous recombination deficient cancer cells (Abbott et al., 2020; Blessing et al., 2020; Hewitt et al., 2021; Juhász et al., 2020; Verma et al., 2021). However, despite thorough biochemical and biophysical scrutiny of its regulation and interaction with nucleosomes (Ahel et al., 2009; Gottschalk et al., 2012, 2009; Lehmann et al., 2020, 2017; Singh et al., 2017), ALC1 has so far resisted structure determination.

Most high-resolution cryo-EM structures of nucleosome-bound chromatin remodelers available to date were obtained with cross-linked complexes (Baker et al., 2021; Farnung et

al., 2020, 2017; Han et al., 2020; He et al., 2020; Li et al., 2019; X. Liu et al., 2017; Patel et al., 2019; Wagner et al., 2020; Yan et al., 2019; Ye et al., 2019). Nonetheless, several structures of non-cross-linked nucleosome-remodeler complexes have attained resolutions of around 4 Å, sufficient to unambiguously assign secondary structure elements and to provide important mechanistic insights. Of these, three were multi-subunit remodeling complexes (Ayala et al., 2018; Eustermann et al., 2018; Willhoft et al., 2018) that may be overall more stable due to multiple interactions between catalytic and scaffolding subunits and the nucleosome, and the remaining three were single-subunit remodelers (Armache et al., 2019; Chittori et al., 2019; Sundaramoorthy et al., 2018). Since PARylation is intrinsically heterogeneous, and since ALC1 physically interacts with at least PAR chains and the nucleosome acidic patch in addition to the nucleosomal DNA, it appears likely that the recognition of a PARylated nucleosome by ALC1 involves stochastically probing these epitopes, visiting a variety of structural states until settling into the active conformation competent for remodeling. Consequently, cross-linking the complex may obscure key information on the recognition process, by turning continuous conformational flexibility into a set of discrete states. Modeling continuous conformational heterogeneity from cryo-EM data is still an open research question, but recent advances in software development suggest that it is now a tractable problem, and that one can circumvent cross-linking (Punjani and Fleet, 2021; Zhong et al., 2021).

Here, we show that PARylated nucleosomes can be efficiently produced *in vitro* with PARP1 or PARP2 and HPF1, and that such nucleosomes are the optimal substrate for ALC1. We reconstituted a complex between ALC1 and a PARylated nucleosome that, in absence of cross-linking, yielded cryo-EM data of sufficient quality to not only permit structure determination of the active state of the nucleosome-bound remodeler, but also to directly visualize multiple conformational states visited during the early events of substrate recognition. Examination of these states identified physical interactions between ALC1 and several nucleosomal epitopes, which our functional assays confirm to be critical for remodeling.

RESULTS

The optimal substrate of ALC1 is a PARylated nucleosome

For structure determination by cryo-EM, we set out to form a stable complex between ALC1 and a nucleosome. At concentrations suitable for cryo-EM sample preparation, the isolated ATPase motor of ALC1 ($ALC1^{cat}$) did not yield any detectable binding to nucleosomes in a gel shift assay (Figure 1A, lane 2). While an essentially full-length protein ($ALC1^{fl}$) did bind to these nucleosomes (Figure 1A, lane 4), this binding predominantly originated from non-specific interactions between its macro domain ($ALC1^{macro}$) and DNA (Figure 1A, lane 3), in agreement with our previous results (Lehmann et al., 2017). In order to explore the impact of nucleosome PARylation on complex formation with ALC1, we repeated these experiments after PARylating the nucleosomes with PARP2 and HPF1 (Bonfiglio et al., 2017). $ALC1^{cat}$ was still unable to bind the PARylated nucleosomes (Figure 1A, lanes 5 and 6), while $ALC1^{macro}$ interacted strongly (Figure 1A, lane 7), consistent with the previously reported K_D of ~11 nM for the interaction between $ALC1^{macro}$ and a tri-(ADP-ribose) model of PAR chains (Singh et al., 2017). The binding of $ALC1^{fl}$ to PARylated nucleosomes resulted in a more defined pattern of shifted bands corresponding to complex formation (Figure 1A, lane 8).

To determine whether the complexes with PARylated or unmodified nucleosomes (Figure 1A, lanes 4 and 8) were functionally different, we adapted a fluorescence resonance energy transfer (FRET)-based nucleosome sliding assay (Yang et al., 2006) (Figure 1B). Rather than adding pre-PARylated PARP1 (auto-modified upon activation with free DNA) to the sliding reaction, we instead used fluorescently labeled and end-positioned nucleosomes to directly activate PARP1. We tested the effect of including or omitting HPF1 in this reaction, leading to PAR chains on both histones and PARP1 or on PARP1 alone, respectively (Bonfiglio et al., 2017). In each case, we first allowed the PARylation reaction to deplete a limiting amount of NAD^+ (Figure S1A), and then added ALC1 and ATP to initiate sliding. Nucleosome sliding by ALC1 was faster (2- to 4-fold) when PAR chains were attached to histones, rather than exclusively to PARP1 (Figure 1B), indicating the PARylated nucleosome is the proper substrate of ALC1. This observation also corroborates the paradigm that in-*trans* ADP-ribosylation of histones, and not only auto-modification of PARP1 and PARP2, is critical to elicit a DNA damage response leading to successful repair and cellular viability (Bonfiglio et al., 2017).

Next, we designed an ALC1-PARylated nucleosome complex amenable to cryo-EM analyses based on the following considerations. The structure of PARP2 and HPF1 bound to nucleosomes indicates that, of the two H3 tails in a nucleosome, the one on the side of the DNA end bound by PARP2 is closest to its active site (Bilokapic et al., 2020). Target residues for ADP-ribosylation (Ser in KS motifs) in this proximal H3 tail should therefore be favored over the equivalent residues in the distal H3 tail. We reasoned that controlling which DNA end PARP2 binds to may yield preferred PARylation of one of the two H3 tails, which may in turn cause ALC1 to preferentially bind to that side of the nucleosome. Conveniently, PARP2 requires a terminal 5'-phosphate group for binding and activation (Langelier et al., 2014; Obaji et al., 2018). We therefore prepared a nucleosome with a 5'-phosphate group at the end of a 10-bp linker DNA on one side, and with a free 5'-hydroxyl at the end of a 0-bp linker DNA on the other side (termed 5'P-10-N-0 nucleosome). This design should strongly favor PARP2 binding to the 10-bp linker, since the 0-bp linker is not only devoid of a terminal 5'-phosphate, but is also sterically unfavorable because of the proximity of the histone octamer. We systematically assessed PARylation conditions to determine the concentrations of PARP2, HPF1 and NAD^+ that maximize PARylation of histones but also limit the auto-modification of PARP2 (Figure S1B). We noticed that high concentrations of HPF1 tend to limit the elongation of PAR chains, a phenomenon also reported and investigated in detail by others (Langelier et al., 2021). Screening micrographs and exploratory 2D and 3D classifications from small screening datasets confirmed that the ALC1-nucleosome complex most amenable to the collection of a large dataset was the one formed with $ALC1^{fl}$ and a 5'P-10-N-0 nucleosome PARylated by PARP2 and HPF1 (Figures 1C, S1C).

Cryo-EM structure of the complex between a PARylated nucleosome and ALC1 in its active state

For structure determination, we collected cryo-EM data of a non-cross-linked complex between $ALC1^{fl}$ and a 5'P-10-N-0 nucleosome PARylated by PARP2 and HPF1. Despite a high level of conformational heterogeneity in our dataset (Figures S2A, S3B and S4), we could isolate a set of 5 487 particles that yielded a map of the ATPase domain of ALC1 bound to the nucleosome with a global resolution of 4.8 Å (Figures 2A and S2A, Table S1). In the absence of cross-linking, only a small number of particles adopted this stable conformation, which limits the attainable resolution. Nevertheless, this resolution is sufficient

for the map to display clear secondary structure elements, allowing model building (Figure 2B). The map reveals an ATPase motor tightly bound to the nucleosomal DNA at superhelical location (SHL) 2 (Figure 2A, 2B), and a clear interaction of the C-terminal ATPase lobe with the N-terminal tail of histone H4 (Figure 2C-F). Both of these features are conserved across almost all chromatin remodelers studied to date (Armache et al., 2019; Chittori et al., 2019; Farnung et al., 2020, 2017; Li et al., 2019; X. Liu et al., 2017; Sundaramoorthy et al., 2018; Wagner et al., 2020; Yan et al., 2019; Ye et al., 2019).

To further examine the conformation of the ALC1 ATPase motor, we compared our model to published structures of nucleosome-bound remodelers from each family of single-subunit remodelers with or without a nucleotide ligand (ADP or ADP-BeF_3): Snf2, Isw1 and CHD4 (Farnung et al., 2020; Li et al., 2019; Yan et al., 2019). We superimposed each of these structures (PDB entries 5Z3L, 5Z3U, 5Z3O, 6JYL, 6IRO and 6RYR) to our model, based on the histone H3 coordinates, which revealed differences in ATPase motor conformations (Figure S3A). The ATPase motor of ALC1 aligns optimally with the ADP-BeF_3 bound conformations of Snf2 and Isw1, compared to their conformations in the presence of ADP or in the absence of any ligand (for Snf2), consistent with our use of this ligand to induce the active conformation of the motor. The ATPase motor of ALC1 is otherwise most similar to that of its closest homologue CHD4.

Notably, our map does not show density for either the macro domain of ALC1 or PAR chains on the nucleosome, most likely due to their extreme conformational flexibility in the active state. However, the average map from a consensus 3D refinement of all 43 698 particles displays clear density for an interaction between ALC1 and the nucleosome acidic patch (Figure 3A), confirming at the structural level and in the context of $ALC1^{fl}$ our previous finding that the acidic patch is important for remodeling by ALC1 (Lehmann et al., 2020). Moreover, this map also features density that we assign to the macro domain (Figure 3A) based on the following rationale: this density makes contact with the ATPase motor, in agreement with the previously reported ATPase motor-macro domain interaction (Lehmann et al., 2017; Singh et al., 2017). Moreover, the density resides on the side of ALC1 directed towards SHL1 where the N-terminal tail of H3 emerges from the two DNA gyres of the nucleosome. The macro domain would thus be positioned at a location compatible with binding to PAR chains at the main PARylation site of the nucleosome (Bonfiglio et al., 2017). Comparing the map of the active state (Figure 2A) with the average map from the larger particle set (Figure 3A) also hints at structural information on additional functional states of the complex.

Analysis of heterogeneity in the cryo-EM data reveals additional functional states of ALC1

Because both 2D classification and 3D variability analysis uncovered continuous conformational heterogeneity in the dataset (Figure S2A), we analyzed it with cryoDRGN (Zhong et al., 2021). We first trained a 256x3 network with a 1-dimensional latent variable on down-sampled images to detect potential contaminants in the set of particles. This approach identified three populations of particles (Figure S3B). Evaluating the decoder at the Z values of these three peaks produced maps very similar to the average map from consensus refinement, indicating that none of these three populations are contaminants (Figure S3B). We then trained a 512x3 network with an 8-dimensional latent variable to analyze the present heterogeneity. The distribution of particles in the latent space is smooth, with no discrete clusters, confirming the heterogeneity to be of a purely continuous conformational nature (Figure 3A). Replicate training runs performed with independent initializations and different network sizes produced comparable results (Figure S4, Table S2). Principal component analysis of the Z values assigned to all particles revealed that the two opposite states along the first principal component of variability correspond to a state with ALC1 tightly bound to SHL2 and the H4 tail (same state described in Figure 2) and a state in which the ATPase domain is only loosely bound to the nucleosomal DNA. We used the graph traversal algorithm implemented in cryoDRGN (Zhong et al., 2021) with intermediate steps chosen to traverse the distribution along the first two principal components, which run approximately parallel to the two UMAP axes in this case (Figure 3A). Because cryo-EM data do not contain temporal information *per se*, this approach cannot inform on kinetics and temporal order. However, because each step of the resulting graph traversal trajectory is supported by observed data, graph traversal enables visualization of plausible conformations visited between these two states (Zhong et al., 2021).

The ATPase domain is highly dynamic along the entire trajectory (Figure 3, Movie M1). Strikingly, we detected states in which the two ATPase lobes are splayed apart in a wide-open conformation (Figure 3B, 3C), similar to the auto-inhibited ATPase motor conformation inferred from SAXS and cross-linking experiments performed in the absence of a nucleosome (Lehmann et al., 2017). In intermediate states, the ATPase domain adopts a closed conformation that resembles the active state conformation but is not as tightly bound to the nucleosomal DNA (Figure 3D, 3E). Finally, cryoDRGN identified states with a closed and tightly bound ATPase motor (Figure 3F, 3G) identical to the active state identified

independently using cryoSPARC 3D variability analysis (Punjani and Fleet, 2021) (Figures 2A, S2A). While the ATPase domain adopts its closed conformation and becomes tightly bound to SHL2, it also samples the nucleosomal DNA around SHL2, approximately from SHL1 to SHL3 (Figure 4, Movies M2 and M3).

The states with an open, loosely bound ATPase domain also feature an interaction with the nucleosome acidic patch (Figure 4B, 4E, Movie M2). This observation is consistent with our earlier discovery of an interaction between the linker region of ALC1 and the acidic patch, and the role of this interaction in regulating ALC1 (Lehmann et al., 2020). Moreover, the density attributed to the macro domain is visible in all these states. Both the acidic patch interaction and the macro domain densities progressively fade away as the ATPase domain transitions to the tightly bound state (Figure 4D-G, Movie M2), indicating that the macro domain and linker occupy less constrained positions when the ATPase domain is in its active conformation. This is in agreement with the model proposed previously, whereby activation of the ATPase requires the disruption of the auto-inhibitory interaction with the macro domain (Lehmann et al., 2017; Singh et al., 2017). We could further detect states with density connecting the nucleosome and macro domain, at a location consistent with the PARylated H3 tail (Figure 4C; also detected in an independent training run, Figure S4B). Finally, the interaction between the C-terminal ATPase lobe of ALC1 and the N-terminal tail of histone H4 is detected in most states, including some in which the ATPase domain is otherwise loosely bound to the DNA (Movie M3). This suggests that this interaction plays a role in recognition, in addition to stimulating the catalytic activity of the ATPase domain as previously shown for other remodelers (Clapier and Cairns, 2012; Hwang et al., 2014; Ludwigsen et al., 2017; Markert et al., 2021; Racki et al., 2014).

Importantly, graph traversal trajectories calculated with different intermediate steps used as anchors reproduced transitions between very similar states. The trajectory presented here therefore likely visualizes the recognition of a PARylated nucleosome by ALC1 leading to its activation (Figures 3, 4, Movies M1, M2, M3).

Nucleosome remodeling by ALC1 depends on its interactions with the acidic patch and the H4 tail

Our structural analysis points to interactions between ALC1 and the PARylated nucleosome as potentially important for productive remodeling; namely interactions between the macro domain and the PAR chains, between the C-ATPase lobe and the H4 tail, and

between the regulatory linker of ALC1 and the nucleosome acidic patch. Previous experiments using PARylated PARP1 or tri-(ADP-ribose) had suggested binding of the macro domain to PAR chains to be required for ATPase activation (Lehmann et al., 2017; Singh et al., 2017). When stimulated by an unmodified nucleosome, even a constitutively active mutant of ALC1, in which the macro domain does not fully inhibit the ATPase ($ALC1^{fl}$ R860W), exhibited reduced ATP hydrolysis rates when compared to a prototypical remodeler like Chd1 (Hauk et al., 2010; Lehmann et al., 2020; Sundaramoorthy et al., 2017). Because the interaction between the macro domain and PAR chains is critical for both binding and activation, we anticipated that disrupting this interface would only result in a fully inactive enzyme. Therefore, we decided to measure nucleosome sliding with PARylated nucleosomes and an unaltered macro domain, while disrupting either the interaction with the H4 tail or that with the acidic patch.

We conducted nucleosome sliding experiments at varying concentrations of ALC1, with or without HPF1 in the PARylation reaction prior to measuring the sliding rates (Figure 5A). When PAR chains were attached to PARP1 but not to the nucleosome (in the absence of HPF1), the sliding reaction followed Michaelis-Menten kinetics with a K_M of 30.7 nM and a V_{max} of 0.11 (a. u.) (Figure 5B). Unexpectedly, this was not the case when PAR chains were attached to the nucleosome (Figure 5B). One likely explanation is that the 63-N-0 end-positioned nucleosomes were preferentially PARylated on the H3 tail proximal to the short DNA end, since the PARP1 molecule bound at the end of the 63-bp linker DNA is too far away to reach the other H3 tail (approximately 214.2 Å away, equivalent to twice the diameter of a nucleosome and therefore too long to be spanned by even a fully extended H3 tail). Asymmetric nucleosome PARylation would result in two binding sites for ALC1 with different affinities: the PARylated side at SHL2 with high affinity for ALC1, and the non-PARylated side at SHL-2 with lower affinity for ALC1. At increasing concentrations of ALC1, the PARylated side would become occupied first and ALC1 would consequently slide the histone octamer away from the Cy5-labeled end. At sufficiently high concentrations of ALC1, a second molecule could engage the weaker second binding site and catalyze sliding in the opposite direction, thereby effectively reducing the net apparent sliding rate. Indeed, a simple model that involves two distinct nucleosomal binding sites with different affinities for ALC1, where the second binding event causes an overall decrease in rate, can in principle explain the markedly non-monotonic shape of the titration curves (Figure S5A; see also Methods). However, the lack of numerical stability in fitting this model to our experimental data prevented us from reliably determining the fit parameters. PARylation of the

nucleosome did not affect the rate of sliding observed at saturating concentrations of ALC1, but instead enhanced sliding rates by ~2.5-fold at low concentrations of ALC1 (Figure 5B). Although we could not determine a K_M value from the data collected in the presence of HPF1, PARylation of the nucleosome appears to decrease K_M when compared to PARylation of PARP1 alone (Figure 5B, Table 1). The overall fastest sliding rate observed in the presence of HPF1 occurs at ~30 nM ALC1, which matches the K_M value determined in the absence of HPF1, indicating that PAR chains contribute to the nucleosome binding affinity of ALC1. This is likely a consequence of the tight binding of the macro domain to PAR chains with a K_D of ~11 nM (Singh et al., 2017), since these PAR chains are covalently attached to the nucleosome rather than merely being in proximity *via* their attachment to PARP1.

To investigate the role of the H4 tail and acidic patch interactions, we constructed two different FRET-labeled end-positioned nucleosomes in addition to WT: a nucleosome with acidic patch mutations (APM nucleosome; alanine substitutions of H2A E61A, E64A, D90A and E92A) and a nucleosome with tail-less (globular) H4 histones (gH4 nucleosome; with a deletion of H4 residues 1-19). Additionally, we used ALC1^{fl} with the two substitutions R611A and S612A within the regulatory linker segment (ALC1^{fl} R611A/S612A) to disrupt the acidic patch interaction on the part of ALC1, as previously (Lehmann et al., 2020). Remodeling by ALC1 was consistently slower at all concentrations of ALC1 tested when using ALC1^{fl} R611A/S612A with WT nucleosomes (Figure 5C), ALC1^{fl} with APM nucleosomes (Figure 5D) or ALC1^{fl} with gH4 nucleosomes (Figure 5E; see also Table 1).

To determine whether the slower remodeling rates observed with gH4 nucleosomes and ALC1^{fl} R611A/S612A were caused by a defect in coupling ATP hydrolysis to the mechanical translocation of DNA around the histone octamer, we measured the ATPase activity of ALC1 stimulated by PARylated nucleosomes (Figures 5F, S5B; see also Methods). Interestingly, the ATPase activity of ALC1 was stimulated to the same extent regardless of whether the PARylation reaction prior to the addition of ATP contained HPF1 or not. This suggests that the increase in sliding rate for nucleosomes PARylated with HPF1 observed with low concentrations of ALC1 (Figure 5B) was not due to more rapid ATP hydrolysis, but rather can be explained by a higher affinity of ALC1 for the PARylated side of the nucleosome. Both the disruption of the acidic patch interaction by the R611A/S612 mutation of ALC1 and the deletion of the H4 tail caused a decrease in ATPase activity by a factor of ~3.5, suggesting that the acidic patch and the H4 tail both regulate ALC1 remodeling primarily by stimulating its ATPase activity.

DISCUSSION

Consistent with the involvement of ALC1 in the DDR triggered by PARylation of chromatin, the establishment of a stable ALC1-nucleosome complex *in vitro* required prior PARylation of the nucleosome substrate. Structures of complexes containing post-translationally modified nucleosomes have been determined before (Anderson et al., 2019; Chatterjee et al., 2015; Hsu et al., 2019; Jang et al., 2019; Kasinath et al., 2021; Lu et al., 2008; Morgan et al., 2016; Sundaramoorthy et al., 2018; Valencia-Sánchez et al., 2021, 2019; Wang et al., 2020b, 2020a; Wilson et al., 2016; Worden et al., 2020, 2019; Xue et al., 2019; Yao et al., 2019), but the present study is, to the best of our knowledge, the first report of a PARylated nucleosome used for structure determination. Cryo-EM data collected on this ALC1-PARylated nucleosome complex in the absence of any cross-linking allowed us to determine the structure of the active state of the ATPase motor of ALC1 bound to the nucleosome. The structure revealed that ALC1 shares two conserved features with other remodelers: its ATPase motor binds to the nucleosomal DNA at SHL2, and the C-ATPase lobe interacts with the N-terminal tail of histone H4. This interaction with the H4 tail was previously shown to be important for remodeling by ALC1, both *in vitro* using gH4 nucleosomes (Ahel et al., 2009) and in cells with the point mutations D377 and D381 in ALC1 (Verma et al., 2021) (Figure S2B). Because we were able to avoid the use of cross-linking due to stabilization of the ALC-nucleosome complex by PARylation, our cryo-EM dataset also captured the ensemble of states ALC1 samples during the recognition of a PARylated nucleosome. Analysis of this heterogeneous ensemble with novel computational methods enabled the direct visualization of these structural states and the possible transitions between them. A subset of the states suggested the location of the macro domain and how it might be positioned to read out PARylation on the H3 tail concomitantly with the ATPase motor engaging its binding site at SHL2. Other states revealed transient interactions between ALC1 and the nucleosome acidic patch, involving a previously identified region of the linker between the ATPase motor and macro domain (Lehmann et al., 2020).

Visualization of these nucleosome epitopes interacting with ALC1 prompted us to measure the effect of their perturbation. This indicated that robust interaction of ALC1 with both the H4 tail and the acidic patch is important for nucleosome sliding, and that the slower rates of sliding observed upon perturbation of these interactions are caused by slower ATP hydrolysis. Remarkably, the slowest rate of ATP hydrolysis measured for ALC1^{fl} stimulated by PARylated gH4 nucleosomes is almost twice as fast as the fastest rate of hydrolysis

measured previously for the constitutively active ALC1^{fl} R860W stimulated by unmodified WT nucleosomes (Lehmann et al., 2020). Moreover, the rate of hydrolysis by ALC1^{fl} stimulated by PARylated WT nucleosomes is more than 6-fold faster than that of ALC1^{fl} R860W stimulated by unmodified WT nucleosomes (Lehmann et al., 2020). This further emphasizes that the *bona fide* substrate of ALC1 is a PARylated nucleosome, eliciting an ATP hydrolysis rate on par with that of Chd1 (Hauk et al., 2010; Sundaramoorthy et al., 2017). Despite these differences in the absolute rate of ATP hydrolysis between these reactions with PARylated or unmodified nucleosomes, the R611A/S612A mutations that disrupt the acidic patch interaction reduce ATP hydrolysis by a similar factor of ~3.5 fold in both settings.

Of note, the asymmetric linker DNA length on the 63-N-0 nucleosome construct used for sliding assays appeared to bias PARylation of histones towards the sites closest to the short DNA end, which in turn affected the directionality of nucleosome sliding by ALC1. This *in vitro* phenomenon likely mimics the processing of a DNA break *in vivo*: in this context, PARP1 or PARP2 would bind to the break and preferentially PARylate target sites closest to it, which would in turn cause ALC1 to slide the PARylated histone octamer away from the DNA break, making it more accessible to downstream repair factors (Figure 6).

In conclusion, our structural and biochemical analyses provide a window into the critical early steps by which, in the context of damaged chromatin, ALC1 recognizes and engages PARylated nucleosomes for productive remodeling (Figure 6). Our work sheds light on the intricate regulatory mechanisms that control the activity of the ALC1 remodeler, which is emerging as an important therapeutic option in HRD-deficient cancers.

MATERIALS AND METHOD

Expression and purification of recombinant proteins

All ALC1 constructs were expressed and purified as described previously (Lehmann et al., 2017). HPF1 was expressed and purified as described in (Gaullier et al., 2020). PARP1 and PARP2 were expressed and purified as described in (Langelier et al., 2017). The pET28a expression vector for PARP2 (isoform 2 with an N-terminal 6-His tag and thrombin cleavage site) was obtained from GenScript. In brief, proteins were expressed in *E. coli* Rosetta 2 (DE3) by addition of IPTG to the culture media. For PARP1 and PARP2, benzamide was added to the expression cultures. Bacterial pellets were harvested by centrifugation, lysed by

sonication, the lysates were cleared by centrifugation and filtration and loaded on a HisTrap HP 5 ml affinity column (Cytiva). Bound proteins were eluted with imidazole, fractions of interest were identified by SDS-PAGE and pooled. As a second step, PARP1 and PARP2 were subjected to affinity chromatography again on a HiTrap Heparin HP 5 ml column (Cytiva) and eluted with a gradient to 1 M NaCl. ALC1 constructs were subjected to ion exchange chromatography on a HiTrap Q HP 5 ml anion exchange column (Cytiva) and a HiTrap SP HP 5 ml cation exchange column (Cytiva) mounted in tandem (Q column to trap contaminating DNA, removed from the circuit before eluting the protein from the SP column with a gradient to 1 M NaCl). HPF1 was directly concentrated and subjected to size exclusion chromatography on a Superdex 75 16/60 column (GE Healthcare), without a second affinity or ion exchange step. ALC1 constructs, PARP1 and PARP2 were concentrated and subjected to size exclusion chromatography on a Superdex 200 16/60 column (GE Healthcare). Pure fractions after size exclusion chromatography were identified by SDS-PAGE, pooled, concentrated and flash frozen in liquid nitrogen before storage at -80ºC.

Nucleosome preparation

Nucleosomal DNA fragments were prepared following the same general strategy as described before (Farnung et al., 2017). In brief, DNA was amplified from a template plasmid containing the 601 sequence (Lowary and Widom, 1998) by PCR in 96-well plates using Phusion polymerase, Phusion HF buffer (New England Biolabs) and each primer at 1 µM (Integrated DNA Technologies). For FRET-labeled nucleosomes, the reverse primer (corresponding to the short linker end) was labeled with Cy5. For labeled DNA, the amplified product was purified using a PrepCell (BioRad). For unlabeled DNA, the amplified product was then purified by anion exchange chromatography on a HiTrap Q HP 1 ml column (Cytiva) by loading 10 ml of pooled PCR reaction on the column at 1 ml/min in 50 mM Tris-HCl pH 8, 100 mM NaCl, 0.1 mM EDTA. Elution was performed with a gradient to 1 M NaCl over 20 column volumes. Adequate fractions were identified by native PAGE on a 10% polyacrylamide gel, pooled, subjected to ethanol precipitation and dissolved in a small volume of pure water. One PCR plate typically yielded around 0.4 mg of DNA.

Purified *Xenopus* histones were purchased from The Histone Source Protein Expression and Purification Facility, Colorado State University, Fort Collins, CO, USA. For FRET-labeled nucleosomes, histone H2A was labeled with Cy3 at position C120 prior to octamer refolding. The histone octamer was refolded by mixing equimolar amounts of H3,

H4, H2A and H2B dissolved in the unfolding buffer (20 mM Tris-HCl pH 7.5, 6 M guanidine HCl, 5 mM DTT) and dialyzing the mixture against refolding buffer (10 mM Tris-HCl pH 7.5, 2 M NaCl, 1 mM EDTA, 5 mM 2-mercaptoethanol) three times over the course of 20 hours. The resulting histone octamer was concentrated and purified by size exclusion chromatography on a Superdex 200 16/60 column (GE Healthcare), and pure fractions were identified by SDS-PAGE (Dyer et al., 2004; Muthurajan et al., 2016). Nucleosomes were assembled by mixing equimolar amounts (as determined by small-scale assembly reactions analyzed by native-PAGE) of histone octamer and DNA in high-salt buffer (10 mM Tris-HCl pH 7.5, 2 M NaCl, 1 mM EDTA, 1 mM DTT) and dialyzing continuously to 0 M NaCl (Dyer et al., 2004; Muthurajan et al., 2016). The nucleosomes were centrifuged at 16 000 xg for 5 min and the supernatant was transferred to a clean tube, to remove precipitated excess histone octamers. Labeled nucleosomes for FRET experiments were additionally purified using a PrepCell (BioRad).

Gel shift assay

Unmodified and PARylated 5'-phosphorylated 10-N-10 nucleosomes were mixed with different ALC1 constructs ($ALC1^{cat}$ residues 16-612; $ALC1^{macro}$ residues 613-879; and $ALC1^{fl}$ residues 16–879) in 1:4 molar ratio in reaction buffer (15 mM HEPES pH 7.5, 50 mM NaCl, 1 mM DTT). The reactions were incubated for an hour on ice. Glycerol was added to the final concentration of ~25% to help load the sample onto 7.5% Mini-PROTEAN® TGX™ Precast Protein Gel (BioRad). The native PAGE was run in the cold room with 0.25x TBE running buffer at 100 V for 150 min. The gel was stained with GelGreen and imaged on a BioRad ChemiDoc MP Imaging System and stained further with InstantBlue.

Ensemble FRET assay for nucleosome remodeling

Nucleosome ensemble remodeling kinetics were measured by monitoring the Cy5 (under 620 nm and 520 nm excitation) and Cy3 (under 520 nm excitation) fluorescence emission signals of a solution of FRET-labeled 63-N-0 nucleosomes using a CLARIOstar (BMG Labtech) multimode microplate reader. Ensemble nucleosome remodeling assays were performed with 10 nM nucleosomes, varying concentrations of $ALC1^{fl}$ as indicated, 1 mM $MgCl_2$ and 50 µM ATP in remodeling buffer (20 mM HEPES pH 7.5, 50 mM KCl, 5 mM $MgCl_2$, 5% sucrose, 0.1 mg/ml BSA, 1 mM DTT). Nucleosomes were PARylated prior to nucleosome remodeling by incubating with 80 nM PARP1, 0 or 20 nM HPF1 and 25 µM

NAD^+ in the remodeling buffer at 37°C for 5 min. Remodeling rates were obtained as initial slopes of the remodeling curves.

Kinetic model

We derived a model similar to the substrate inhibition model developed by Haldane (Armstrong, 1930; Reed et al., 2010). This model assumes that remodeler-nucleosome binding is at equilibrium and that the Michaelis constants for the two binding sites, K_1 and K_2, satisfy $K_2 >> K_1$, such that binding can be considered sequential. The model also assumes that [ALC1] >> [nucleosome]. The net apparent sliding rate V is then given by

$$V = \frac{V_2 \times [ALC1]^2 + V_1 \times K_2 \times [ALC1]}{[ALC1]^2 + K_2 \times [ALC1] + K_1 \times K_2}$$

where V_1 and V_2 are the maximum sliding rates for the two opposing remodeling directions.

ATPase assay

ATPase activity was measured using a coupled enzyme system in which regeneration of hydrolyzed ATP is coupled to NADH oxidation as described previously (Nørby, 1988). The assay follows NADH absorbance at 340 nm. Final concentrations of 0.45 mM NADH, 1.0 mM phosphoenolpyruvate, 54 U/ml pyruvate kinase (Sigma), and 78 U/ml lactic dehydrogenase (Sigma) were used. For measurements of nucleosome-stimulated ATPase activity, reactions contained 2 µM $ALC1^{fl}$, 250 nM nucleosomes, and 1 mM ATP in a volume of 30 µl in the reaction buffer (20 mM HEPES pH 8, 25 mM NaCl, 75 mM KCl, 1 mM $MgCl_2$). Nucleosomes were PARylated prior measurements with 2 µM PARP1, 0.5 µM HPF1 and 25 µM NAD^+ for 5 min at 37ºC. After PARylation, Olaparib was added at a final concentration of 4 µM. Absorbance at 340 nm was monitored at 37ºC using a CLARIOstar microplate reader (BMG Labtech) and clear low-volume 384-well microplates (Greiner). The decrease in the absorbance [$\Delta A_{340}/\Delta t$] is converted to ATPase activity [ATP/s/enzyme] by using 6.22 $mM^{-1}cm^{-1}$ as extinction coefficient of NADH at 340 nm.

Importantly, this reporter reaction produces NAD^+ (Figure S5B), which in our specific case is an undesired side effect. Since PARylation reactions performed prior to ATP hydrolysis rate measurements contain PARP1, and the extent of PARylation is controlled by providing a limiting amount of NAD^+, any newly formed NAD^+ from the reporter reaction may be used by PARP1 with two possible, undesired consequences: first, PARP1 may further modify the nucleosome over the course of the reaction, thereby changing the substrate of

ALC1 as the reaction of interest progresses; second, in doing so or even simply by hydrolyzing NAD^+ to ADP-ribose and nicotinamide, PARP1 may shift the equilibrium of the reporter reaction and artificially increase its rate with no relation to the rate of ATP hydrolysis under study. To control for these effects, we performed the reaction in the absence and presence of Olaparib, a clinical PARP inhibitor. When omitting Olaparib, the observed rate of ATP hydrolysis is indeed faster than in reactions containing the inhibitor added after the intended PARylation has completed, but before addition of ATP (Figure S5B, compare blue curve to yellow and green curves). When omitting NAD^+ in the initial PARylation reaction and adding Olaparib before ATP is introduced, ATP hydrolysis occurs at baseline rate during the first 10 min, and eventually speeds up to the same rate as catalyzed by ALC1 (Figure S5B, compare red curve to yellow and green curves). This sudden speed up is likely caused by PARP1 overcoming inhibition once enough NAD^+ has accumulated at baseline rate, and ALC1 activating once PARP1 has produced PAR chains long enough, which would presumably happen fast since PAR chains only three ADP-ribose units long are sufficient for full activation of ALC1 (Singh et al., 2017).

Preparation of PARylated nucleosomes

Initial PARylation conditions were chosen to form a fully saturated HPF1-PARP2-nucleosome or HPF1-PARP1-nucleosome complex, based on the K_D values for the PARP2-nucleosome and HPF1-PARP2-nucleosome interactions reported in (Gaullier et al., 2020), and based on reaction conditions reported in (Bilokapic et al., 2020). We used a nucleosome with 10-bp linker DNA ends on both sides (10-N-10). For reactions with PARP2, we used the same nucleosome with a terminal 5'-phosphate group at one end (5'P-10-N-10), since PARP2 requires it for binding and activation (Langelier et al., 2014; Obaji et al., 2018). Reactions were initiated by the addition of NAD^+ after pre-formation of the HPF1-PARP-nucleosome complex, and reaction products were analyzed by Western blot using a pan-ADP-ribose antibody (Abcam, ab14459). Titrations of NAD^+ and PARP/HPF1 were analyzed to determine the concentrations of components giving a strong PARylation signal on histones while keeping auto-PARylation of PARP as limited as possible. Nucleosomes PARylated with PARP2 displayed shorter PAR chains, as assessed from screening micrographs, and were therefore most suitable for cryo-EM, while nucleosomes for remodeling assays and ATPase assays were PARylated with PARP1 because they did not have a terminal 5'-phosphate group required by PARP2.

Western blot

Reactions were prepared in 30 µl in the assay buffer (25 mM HEPES-NaOH pH 8.0, 50 mM NaCl, 0.1 mM EDTA, 0.1 mM TCEP). Nucleosomes at 1 µM final concentration were incubated with PARP1 or PARP2 and HPF1 in the molar ratios as indicated above the panels (Figure S1B). For the initial three experiments; varying HPF1, PARP1 and PARP1:HPF1 amounts (panel 1-3), NAD^+ was added at the final concentration of 6.25 mM. For NAD^+ titration, NAD^+ was added in the gradient from 0.1 to 12.8 mM (panel 4), and from 150 to 225 uM in 25 uM steps (panel 5). Reactions were incubated 30 min on ice or 10ºC as indicated. After incubation time, reactions were split and loaded onto two identical 4-20% Mini-PROTEAN® TGX™ Precast Protein Gels (BioRad). Proteins were separated by SDS-PAGE at 120 V for 90 min. One gel was stained with InstantBlue Coomassie stain and the other was used for protein immunoblotting. Proteins were transferred onto 0.2 µm nitrocellulose blotting membranes (Cytiva) by wet electro transfer at constant 20 V overnight in the cold room. Transfer efficiency was confirmed by staining with 0.1% w/v Ponceau in 5% acetic acid. Membranes were blocked with 5% skim milk/TBS-T (1xTBS Tween-20) for 1 h at room temperature and probed with mouse monoclonal Anti-Poly (ADP-Ribose) Polymer (Abcam, ab14459) primary antibody overnight at 4°C. Membranes were then washed 3 times for 5 min with TBS-T, incubated with goat anti-mouse (Abcam, ab205719) secondary antibody conjugated to a horseradish peroxidase (HRP) for 1 h at room temperature and washed again 3 times for 5 min with TBS-T. Immunoblots were developed using Clarity Western ECL Substrate (Bio-Rad).

Cryo-EM sample preparation

The sample was prepared as follows: an initial mixture of 5'P-10-N-0 nucleosome at 1 µM, PARP2 at 1 µM and HPF1 at 4 µM was incubated on ice for 30 min before addition of NAD^+ to 200 µM and further incubation at 10ºC for 60 min to allow PARylation until the reaction ends (either because it exhausts the limiting amount of NAD^+, or because auto-modified PARP2 dissociates from the nucleosome). $ALC1^{fl}$ was then added to a final concentration of 3 µM, and ADP-BeF_3 to a final concentration of 1 mM (1x). The mixture was further incubated on ice for 50 min before vitrification. ADP-BeF_3 was prepared as a 10x stock (10 mM ADP, 30 mM $BeSO_4$, 150 mM NaF, 10 mM $MgCl_2$), freshly before use.

Quantifoil R 2/2 Cu 200 grids (Electron microscopy sciences) were glow-discharged at 20 mA and 0.4 mbar with negative polarity for 60 s in a PELCO easiGlow glow

discharger. 3 µl of the sample was applied onto grids and immediately blotted for 2.5 s. Grids were plunge-frozen into liquid ethane using a Vitrobot Mark IV (Thermo Fisher Scientific) operated at 100% relative humidity and 4ºC.

Cryo-EM data collection and processing

Cryo-EM data were collected at the SciLifeLab facility in Stockholm, Sweden, on a Titan Krios equipped with a Gatan K3 detector operated in counting mode and an energy filter with a slit width of 20 eV. Magnification was 105kx, resulting in an image pixel size of 0.84 Å/pixel. A total accumulated dose of 45 $e^-/Å^2$ was fractionated in 40 movie frames. Movies were motion-corrected using UCSF MotionCor2 (Zheng et al., 2017) and CTF parameters were estimated using CTFFIND4 (Rohou and Grigorieff, 2015), both from within RELION version 3.1.1 (Zivanov et al., 2018). Particle-picking was done using Topaz (Bepler et al., 2019). A relatively homogeneous set of 43 698 particles could be isolated by several rounds of 2D and 3D classification in RELION. The 3D reference used for the first 3D classification was a synthetic map generated from a nucleosome atomic model from PDB entry 3LZ0 (Vasudevan et al., 2010) using a low-pass filter to 30 Å resolution. Subsequent 3D classifications used the best map from the previous round as 3D reference. Details are provided in Figure S2.

Identification and 3D refinement of the active state of the ALC1-nucleosome complex

The map resulting from 3D refinement of the 43 698 particles showed signs of continuous conformational heterogeneity in the region of ALC1, notably with alpha helices appearing as flattened stretches of density instead of cylinders (as alpha helices in histones). Accordingly, attempts at improving the ALC1 density using multi-body refinement in RELION (Nakane et al., 2018) were unsuccessful, yielding only deteriorated maps for this body. This further suggested that this dataset does not meet the assumption underlying this approach that the whole particle is composed of several rigid bodies, meaning that ALC1 undergoes conformational changes. We imported these particles into cryoSPARC (Punjani et al., 2017) at their original pixel size of 0.84 Å/pixel with a box size of 512 pixels, and Fourier cropped them to a box size of 400 pixels. We ran homogeneous refinement with automatic masking to generate an appropriate mask for 3D variability analysis (3DVA). We then subjected these particles to 3DVA (Punjani and Fleet, 2021), solving for three principal

components and with a filter resolution of 4 Å; all other parameters were left with their default values. The resulting distributions along the principal components of variability were smooth, confirming both the compositional homogeneity of this set of particles and the presence of conformational flexibility (Figure S2A). Notably, the trajectory along PC1 revealed that the first source of variability in the dataset is the presence of two binding modes of ALC1 to the nucleosomes: one in which the ATPase motor is loosely bound to the DNA and the remodeler makes an interaction with the acidic patch, the other in which the ATPase motor is tightly associated with the DNA at SHL2 and with no visible interaction with the acidic patch. We call this latter state the "active state", based on previous literature on chromatin remodelers and since this tightly bound ATPase motor is a requirement for remodeling activity. Clustering particles based on their latent coordinates from 3DVA into 5 subpopulations isolated a set of 5 487 particles that gave an improved reconstruction of the active state of ALC1. These particles were finally subjected to non-uniform refinement (Punjani et al., 2020), which yielded a map of the active state with a global resolution of 4.8 Å (Figure 2A) and small variations in local resolution (Figure S2A).

Analysis of heterogeneity in the cryo-EM dataset

Given the evidence that the set of 43 698 still contained significant continuous heterogeneity, we then analyzed it with cryoDRGN (Zhong et al., 2021). All models were trained for 50 epochs on a single GPU. We re-extracted these particles in RELION with a box size of 128 pixels and a pixel size of 3.36 Å/pixel for rapid evaluation. We first trained a cryoDRGN model on these downsampled particles with 3 layers and 256 nodes per layer for both the encoder and decoder network architectures (termed 256x3) and a 1-dimensional latent variable Z. This resulted in three major populations of particles, based on Z values. Evaluating the decoder at the most populated Z values yielded recognizable maps of the complex, indicating that none of these populations were "junk" particles and confirming that our strict selections between rounds of 3D classifications yielded a clean set of particles. Next, we trained a 256x3 model on these same particles, this time with an 8-dimensional latent variable Z to analyze heterogeneity. We trained this model three times with independent initializations. For all three replicate runs, the resulting distribution of Z values is smooth, indicating that heterogeneity in the dataset originates purely from continuous conformational changes and not from populations of particles with distinct compositions, in agreement with the 3DVA results. We then sampled the resulting distributions of Z values

using k-means clustering with 20 cluster centers, as implemented in cryoDRGN. The resulting maps show a variety of states, including states with a tightly bound ATPase domain similar to the active state we could build an atomic model for, and states with a loosely bound ATPase motor and visible interaction with the acidic patch. Finally, we re-extracted the particles with a box size of 128 pixels and a pixel size of 1.68 Å/pixel to get higher resolution reconstructions. This resulted in a smaller physical box size (128 pixels at 1.68 Å/pixel, resulting in a box 215 Å wide), which in this case was beneficial since the initial box (128 pixels at 3.36 Å/pixel, resulting in a box 430 Å wide) was wide enough to enclose neighboring particles. A trial-and-error exploration of box size and pixel size parameters gave more interpretable maps when using the same box size in pixels with smaller pixels (resulting in a smaller physical box size) than when compensating for smaller pixels by increasing the box size in pixels in order to keep the same physical box size. Tighter boxes tended to give better results because the encoder network of cryoDRGN is presented with the entire, unmasked box, and larger boxes were more likely to contain neighboring particles around the particle of interest at the center of the box, artificially increasing the heterogeneity detected by the encoder.

Model building and refinement

We generated a homology model of the ALC1 ATPase domain using SWISS-MODEL (Waterhouse et al., 2018). The structure of ISWI from PDB entry 6JYL (Yan et al., 2019) provided the template that gave the best-scoring model according to SWISS-MODEL's metrics. We used the nucleosome model from PDB entry 6RYR (Farnung et al., 2020). These two models were placed into the map of the active state using UCSF ChimeraX version 1.1 (Goddard et al., 2018; Pettersen et al., 2021) and subjected to three rounds of interactive molecular dynamics flexible fitting (iMDFF) using ISOLDE version 1.1 (Croll, 2018) followed by real-space refinement in phenix.real_space_refine (Afonine et al., 2018). Model-to-map real space correlation coefficients and model geometry statistics were calculated with phenix.validation_cryoem. All Phenix programs used were from the Phenix suite version 1.19.2-4158 (Liebschner et al., 2019).

DATA AVAILABILITY

The cryo-EM map of the ALC1-nucleosome complex in the active state was deposited at the EMDB with accession code EMD-13065. The model of the ALC1-nucleosome complex in

the active state was deposited at the PDB with accession code 7OTQ. The map series from the cryoDRGN graph traversal was deposited at the EMDB with accession code EMD-13070.

ACKNOWLEDGMENTS

Cryo-EM data were collected at the Swedish National Cryo-EM Facility funded by the Knut and Alice Wallenberg, Family Erling Persson and Kempe Foundations, SciLifeLab, Stockholm University and Umeå University. We thank M. Carroni, K. Wallden, and J. Conrad for assistance with cryo-EM data collection, and H. Schüler for discussions and for providing reagents. We thank J. Pascal for generously providing the PARP1 expression vector. The HPF1 expression vector was a kind gift from K. Luger. We thank M. Schattenhofer for assistance with figure layout. This work was supported by the European Research Council (ERC Starting Grant 714068), the Knut and Alice Wallenberg Foundation (Grant KAW 019.0306), the Swedish Research Council (VR Grant 2019-03534), and Cancerfonden (Grant 19 0055 Pj). S.D. is an EMBO Young Investigator. G.H. and S.J.B. are supported by the Francis Crick Institute, which receives its core funding from Cancer Research UK (FC0010048), the UK Medical Research Council (FC0010048) and the Wellcome Trust (FC0010048); S.J.B. is also funded by a European Research Council (ERC) Advanced Investigator Grant (TelMetab); and Wellcome Trust Senior Investigator and Collaborative Grants.

AUTHOR CONTRIBUTIONS

S.D. conceived and oversaw the study; L.B., G.G., A.S., L.C.L., K.B., D.D., S.J.B. and S.D. designed, and/or conducted/analyzed experiments; L.B. collected cryo-EM data, with help from G.G; G.G. analyzed cryo-EM data, with help from L.B. and input from M.H. during the initial stages; G.G. and S.D. wrote the manuscript with help from S.J.B. and G.H., and editorial input from all other authors.

COMPETING INTERESTS

S.J.B. is co-founder and VP Science Strategy at Artios Pharma Ltd.

FIGURE LEGENDS

Figure 1. Identification of an ALC1 - PARylated nucleosome complex suitable for cryo-EM.

(A) EMSA analysis of the complexes formed by different constructs of ALC1 and a 10-N-10 nucleosome in absence or presence of PAR chains deposited by PARP2 and HPF1.

(B) Nucleosome sliding assay of 10 nM nucleosomes by 31.3 nM ALC1^{fl}, performed after PARylation by 80 nM of PARP1 with 25 µM NAD^+ in absence (teal) and presence (orange) of 20 nM of HPF1.

(C) Preparation and native PAGE analysis of the complex between ALC1^{fl} and a PARylated nucleosome for cryo-EM (see Methods).

Figure 2. Cryo-EM structure of the complex between a PARylated nucleosome and ALC1 in its active state.

(A) Cryo-EM map of the complex between a PARylated nucleosome and ALC1 in the state tightly bound to SHL2 and the H4 tail. The map is shown at a contour level of 0.15 and colored by chain assignment (H3 in blue, H4 in green, H2A in yellow, H2B in red, DNA in grey and ALC1 in pink). The black ellipse in the dyad view indicates the nucleosome dyad axis.

(B) Atomic model of the complex between a PARylated nucleosome and ALC1 in the state tightly bound to SHL2 and the H4 tail. Same views and same color code as in (A). The black ellipse in the dyad view indicates the nucleosome dyad axis.

(C) Same cryo-EM map as in (A), displayed at the same contour level, but in two different orientations, showing the H4 tail interacting with the C-terminal ATPase domain of ALC1. Same color code as in (A).

(D) Close-up view of the boxed region in (C).

(E) Atomic model shown in the same two orientations as in (C). In addition to the same color code as in (A), the cryo-EM density of the H4 tail is shown as a turquoise transparent surface, at the same contour level as in (A), (C) and (D).

(F) Close-up view of the boxed region in (E).

Figure 3. Dynamics of the ATPase domain of ALC1.

(A) Left: consensus map from 3D refinement in RELION of 43 698 particles, displayed at a contour level of 0.015 and in disc view. Regions of the map assigned to an interaction with the nucleosome acidic patch and to the macro domain are labeled. Right: UMAP visualization of the latent variable distribution of these same 43 698 particle images after training of an 8-dimensional latent variable model with cryoDRGN. Dots indicate all latent space coordinates that are part of the calculated graph traversal, labeled red dots indicate coordinates of maps shown in panels (B) to (G). Black lines are a visual guide and do not represent actual connectivity of the graph traversal.

(B) to (G) Maps sampled at representative steps along the graph traversal shown in (A). All maps are displayed at a contour level of 0.025 and in gyres view.

Figure 4. Dynamics of the acidic patch interacting region and macro domain of ALC1.

(A) Left: consensus map from 3D refinement in RELION of 43 698 particles, displayed at a contour level of 0.015 and in disc view. Regions of the map assigned to an interaction with the nucleosome acidic patch and to the macro domain are labeled (same panel as in Figure 3A). Right: same plot as in Figure 3A but sampling different steps along the same graph traversal. Dots indicate all latent space coordinates that are part of the calculated graph traversal, labeled red dots indicate coordinates of maps shown in panels (B) to (G). Black lines are a visual guide and do not represent actual connectivity of the graph traversal.

(B) to (G) Maps sampled along the graph traversal shown in (A). All maps are displayed at a contour level of 0.013 and in disc view.

Figure 5. ALC1 kinetics in nucleosome sliding and ATPase assays.

(A) Left: schematic of asymmetric nucleosomes PARylated by PARP1 with and without HPF1. Right: adding ALC1 and ATP to the FRET-labeled nucleosome results in shifting DNA away from a shorter linker side which results in a decrease of FRET efficiency.

(B) Saturation curves of nucleosome sliding rates for 10 nM WT nucleosomes versus varying concentrations of ALC1^{fl}. Nucleosome sliding assays were performed after PARylation by 80 nM PARP1 with 25 μM NAD$^+$ in the absence (teal) or presence (orange) of 20 nM of HPF1. Error bars represent SD (N = 3 independent experiments).

(C) Saturation curve of nucleosome sliding rates for 10 nM WT nucleosomes versus varying concentrations of ALC1^{fl} R611A/S612A. Nucleosome sliding assays were performed after PARylation by 80 nM PARP1 and 20 nM HPF1 with 25 μM NAD$^+$. Error bars represent SD (N = 3 independent experiments).

(D) and (E) Saturation curves of nucleosome sliding rates for 10 nM APM (D) and gH4 (E) nucleosomes versus varying concentrations of ALC1^{fl}. Nucleosome sliding assays were performed after PARylation by 80 nM PARP1 and 20 nM HPF1 with 25 μM NAD$^+$. Error bars represent SD (N = 3 independent experiments).

(F) ATPase activity for 2 μM ALC1^{fl} (teal, orange, and green) or ALC1^{fl} R611A/S612A (blue) in the presence of 250 nM 10-N-10 WT nucleosomes (teal, orange, and blue) or 10-N-10 gH4 nucleosomes (green), activated by PARylation by PARP1 with (orange, blue, and green) or without HPF1 (teal). Error bars represent SD from a minimum of 2 independent experiments.

Figure 6. Model for the recognition of a PARylated nucleosome by ALC1.

Upon DNA damage, PARP1 and HPF1 deposit PAR chains on histones, causing the rapid recruitment of proteins containing PAR reader domains. Among these proteins, ALC1 selectively binds to PAR chains with its macro domain and recognizes the closest nucleosome by probing its acidic patch. Once the macro domain and linker region of ALC1 jointly recognize a PARylated nucleosome, the ATPase motor is released from their auto-inhibitory effect and can tightly bind to the nucleosomal DNA at SHL2 for productive remodeling. Preferential PARylation of target sites spatially closest to the DNA break causes preferential recruitment of ALC1 on the side of the nucleosome such that remodeling slides this nucleosome away from the break. By setting directionality in remodeling, this mechanism could promote exposure of the lesion to downstream repair factors.

TABLES

Condition	Sliding rate (a.	[ALC1] at peak	Sliding rate at	Sliding rate at

	u.) at [ALC1] = 31.25 nM	(nM)	peak (a.u.)	saturation ([ALC1] = 2 µM)
-HPF1	0.059 ± 0.002	NA	NA	0.101 ± 0.015
+HPF1	0.144 ± 0.009	31.25	0.144 ± 0.009	0.102 ± 0.016
+HPF1, ALC1^{fl} R611A, S612A	0.085 ± 0.025	62.50	0.110 ± 0.003	0.068 ± 0.014
+HPF1, APM nuc	0.029 ± 0.009	250.00	0.075 ± 0.003	0.032 ± 0.009
+HPF1, gH4 nuc	0.038 ± 0.004	125.00	0.091 ± 0.010	0.022 ± 0.002

Table 1. Kinetic parameters from nucleosome sliding assays. Rates are expressed as the mean ± standard deviation from three independent measurements (NA: not applicable).

SUPPLEMENTARY INFORMATION

Supplementary Information includes 5 Figures, 2 Tables, and 3 Movies.

Movie M1. Related to Figure 3. Dynamics of the ATPase lobes of ALC1.

Movie M2. Related to Figure 4. Dynamics of the acidic patch interacting region and macro domain of ALC1.

Movie M3. Related to Figure 4. Dynamics of the H4 tail interaction.

REFERENCES

Abbott JM, Zhou Q, Esquer H, Pike L, Broneske TP, Rinaldetti S, Abraham AD, Ramirez DA, Lunghofer PJ, Pitts TM, Regan DP, Tan A-C, Gustafson DL, Messersmith WA, LaBarbera DV. 2020. First-in-Class Inhibitors of Oncogenic CHD1L With Preclinical Activity Against Colorectal Cancer. *Mol Cancer Ther*. doi:10.1158/1535-7163.MCT-20-0106

Afonine PV, Poon BK, Read RJ, Sobolev OV, Terwilliger TC, Urzhumtsev A, Adams PD. 2018. Real-space refinement in PHENIX for cryo-EM and crystallography. *Acta Crystallogr Sect Struct Biol* **74**:531–544. doi:10.1107/S2059798318006551

Ahel D, Hořejší Z, Wiechens N, Polo SE, Garcia-Wilson E, Ahel I, Flynn H, Skehel M, West SC, Jackson SP, Owen-Hughes T, Boulton SJ. 2009. Poly(ADP-ribose)–Dependent Regulation of DNA Repair by the Chromatin Remodeling Enzyme ALC1. *Science* **325**:1240–1243. doi:10.1126/science.1177321

Anderson CJ, Baird MR, Hsu A, Barbour EH, Koyama Y, Borgnia MJ, McGinty RK. 2019. Structural Basis for Recognition of Ubiquitylated Nucleosome by Dot1L Methyltransferase. *Cell Rep* **26**:1681-1690.e5. doi:10.1016/j.celrep.2019.01.058

Armache JP, Gamarra N, Johnson SL, Leonard JD, Wu S, Narlikar GJ, Cheng Y. 2019. Cryo-EM structures of remodeler-nucleosome intermediates suggest allosteric control through the nucleosome. *eLife* **8**:e46057. doi:10.7554/eLife.46057

Armstrong EF. 1930. Enzymes. By J.B.S. Haldane, M.A. Monographs on Biochemistry. Edited by R.H.A. Plimmer, D.Sc., and Sir F. G. Hopkins, M.A., M.B., D.Sc., F.R.S. Pp. vii+235. London: Longmans, Green & Co., 1930. Price 14s. *J Soc Chem Ind* **49**:919–920. doi:https://doi.org/10.1002/jctb.5000494433

Ayala R, Willhoft O, Aramayo RJ, Wilkinson M, McCormack EA, Ocloo L, Wigley DB, Zhang X. 2018. Structure and regulation of the human INO80–nucleosome complex. *Nature* **556**:391–395. doi:10.1038/s41586-018-0021-6

Baker RW, Reimer JM, Carman PJ, Turegun B, Arakawa T, Dominguez R, Leschziner AE. 2021. Structural insights into assembly and function of the RSC chromatin remodeling complex. *Nat Struct Mol Biol* **28**:71–80. doi:10.1038/s41594-020-00528-8

Bepler T, Morin A, Rapp M, Brasch J, Shapiro L, Noble AJ, Berger B. 2019. Positive-unlabeled convolutional neural networks for particle picking in cryo-electron micrographs. *Nat Methods* 1–8. doi:10.1038/s41592-019-0575-8

Bilokapic S, Suskiewicz MJ, Ahel I, Halic M. 2020. Bridging of DNA breaks activates PARP2–HPF1 to modify chromatin. *Nature* 1–5. doi:10.1038/s41586-020-2725-7

Blessing C, Mandemaker IK, Gonzalez-Leal C, Preisser J, Schomburg A, Ladurner AG. 2020. The Oncogenic Helicase ALC1 Regulates PARP Inhibitor Potency by Trapping PARP2 at DNA Breaks. *Mol Cell* **80**:862-875.e6. doi:10.1016/j.molcel.2020.10.009

Bonfiglio JJ, Fontana P, Zhang Q, Colby T, Gibbs-Seymour I, Atanassov I, Bartlett E, Zaja R, Ahel I, Matic I. 2017. Serine ADP-Ribosylation Depends on HPF1. *Mol Cell* **65**:932-940.e6. doi:10.1016/j.molcel.2017.01.003

Chatterjee N, North JA, Dechassa ML, Manohar M, Prasad R, Luger K, Ottesen JJ, Poirier MG, Bartholomew B. 2015. Histone Acetylation near the Nucleosome Dyad Axis Enhances Nucleosome Disassembly by RSC and SWI/SNF. *Mol Cell Biol* **35**:4083–4092. doi:10.1128/MCB.00441-15

Chittori S, Hong J, Bai Y, Subramaniam S. 2019. Structure of the primed state of the ATPase domain of chromatin remodeling factor ISWI bound to the nucleosome. *Nucleic Acids Res* **47**:9400–9409. doi:10.1093/nar/gkz670

Clapier CR, Cairns BR. 2012. Regulation of ISWI involves inhibitory modules antagonized by nucleosomal epitopes. *Nature* **492**:280–284. doi:10.1038/nature11625

Croll TI. 2018. ISOLDE: a physically realistic environment for model building into low-resolution electron-density maps. *Acta Crystallogr Sect Struct Biol* **74**. doi:10.1107/S2059798318002425

Dyer PN, Edayathumangalam RS, White CL, Bao Y, Chakravarthy S, Muthurajan UM, Luger K. 2004. Reconstitution of nucleosome core particles from recombinant histones and DNA. *Methods Enzymol* **375**:23–44. doi:10.1016/s0076-6879(03)75002-2

Eustermann S, Schall K, Kostrewa D, Lakomek K, Strauss M, Moldt M, Hopfner K-P. 2018. Structural basis for ATP-dependent chromatin remodelling by the INO80 complex. *Nature* **556**:386–390. doi:10.1038/s41586-018-0029-y

Farnung L, Ochmann M, Cramer P. 2020. Nucleosome-CHD4 chromatin remodeller structure maps human disease mutations. *eLife* **9**:e56178. doi:10.7554/eLife.56178

Farnung L, Vos SM, Wigge C, Cramer P. 2017. Nucleosome–Chd1 structure and implications for chromatin remodelling. *Nature* **550**:539–542. doi:10.1038/nature24046

Gaullier G, Roberts G, Muthurajan UM, Bowerman S, Rudolph J, Mahadevan J, Jha A, Rae PS, Luger K. 2020. Bridging of nucleosome-proximal DNA double-strand breaks by

PARP2 enhances its interaction with HPF1. *PLOS ONE* **15**:e0240932. doi:10.1371/journal.pone.0240932

Goddard TD, Huang CC, Meng EC, Pettersen EF, Couch GS, Morris JH, Ferrin TE. 2018. UCSF ChimeraX: Meeting modern challenges in visualization and analysis. *Protein Sci* **27**:14–25. doi:10.1002/pro.3235

Gottschalk AJ, Timinszky G, Kong SE, Jin J, Cai Y, Swanson SK, Washburn MP, Florens L, Ladurner AG, Conaway JW, Conaway RC. 2009. Poly(ADP-ribosyl)ation directs recruitment and activation of an ATP-dependent chromatin remodeler. *Proc Natl Acad Sci* **106**:13770–13774. doi:10.1073/pnas.0906920106

Gottschalk AJ, Trivedi RD, Conaway JW, Conaway RC. 2012. Activation of the SNF2 Family ATPase ALC1 by Poly(ADP-ribose) in a Stable ALC1·PARP1·Nucleosome Intermediate. *J Biol Chem* **287**:43527–43532. doi:10.1074/jbc.M112.401141

Han Y, Reyes AA, Malik S, He Y. 2020. Cryo-EM structure of SWI/SNF complex bound to a nucleosome. *Nature* 1–4. doi:10.1038/s41586-020-2087-1

Hauk G, McKnight JN, Nodelman IM, Bowman GD. 2010. The Chromodomains of the Chd1 Chromatin Remodeler Regulate DNA Access to the ATPase Motor. *Mol Cell* **39**:711–723. doi:10.1016/j.molcel.2010.08.012

He S, Wu Z, Tian Y, Yu Z, Yu J, Wang X, Li J, Liu B, Xu Y. 2020. Structure of nucleosome-bound human BAF complex. *Science* **367**:875–881. doi:10.1126/science.aaz9761

Hewitt G, Borel V, Segura-Bayona S, Takaki T, Ruis P, Bellelli R, Lehmann LC, Sommerova L, Vancevska A, Tomas-Loba A, Zhu K, Cooper C, Fugger K, Patel H, Goldstone R, Schneider-Luftman D, Herbert E, Stamp G, Brough R, Pettitt S, Lord CJ, West SC, Ahel I, Ahel D, Chapman JR, Deindl S, Boulton SJ. 2021. Defective ALC1 nucleosome remodeling confers PARPi sensitization and synthetic lethality with HRD. *Mol Cell* **81**:767-783.e11. doi:10.1016/j.molcel.2020.12.006

Hsu PL, Shi H, Leonen C, Kang J, Chatterjee C, Zheng N. 2019. Structural Basis of H2B Ubiquitination-Dependent H3K4 Methylation by COMPASS. *Mol Cell*. doi:10.1016/j.molcel.2019.10.013

Hwang WL, Deindl S, Harada BT, Zhuang X. 2014. Histone H4 tail mediates allosteric regulation of nucleosome remodelling by linker DNA. *Nature* **512**:213–217. doi:10.1038/nature13380

Jang S, Kang C, Yang H-S, Jung T, Hebert H, Chung KY, Kim SJ, Hohng S, Song J-J. 2019. Structural basis of recognition and destabilization of the histone H2B ubiquitinated nucleosome by the DOT1L histone H3 Lys79 methyltransferase. *Genes Dev*. doi:10.1101/gad.323790.118

Juhász S, Smith R, Schauer T, Spekhardt D, Mamar H, Zentout S, Chapuis C, Huet S, Timinszky G. 2020. The chromatin remodeler ALC1 underlies resistance to PARP inhibitor treatment. *Sci Adv* **6**:eabb8626. doi:10.1126/sciadv.abb8626

Kasinath V, Beck C, Sauer P, Poepsel S, Kosmatka J, Faini M, Toso D, Aebersold R, Nogales E. 2021. JARID2 and AEBP2 regulate PRC2 in the presence of H2AK119ub1 and other histone modifications. *Science* **371**. doi:10.1126/science.abc3393

Krishnakumar R, Kraus WL. 2010. The PARP Side of the Nucleus: Molecular Actions, Physiological Outcomes, and Clinical Targets. *Mol Cell* **39**:8–24. doi:10.1016/j.molcel.2010.06.017

Langelier M-F, Billur R, Sverzhinsky A, Black BE, Pascal JM. 2021. HPF1 dynamically controls the PARP1/2 balance between initiating and elongating ADPribose modifications. *bioRxiv* 2021.05.19.444852. doi:10.1101/2021.05.19.444852

Langelier M-F, Riccio AA, Pascal JM. 2014. PARP-2 and PARP-3 are selectively activated by 5′ phosphorylated DNA breaks through an allosteric regulatory mechanism shared with PARP-1. *Nucleic Acids Res* **42**:7762–7775. doi:10.1093/nar/gku474

Langelier M-F, Steffen JD, Riccio AA, McCauley M, Pascal JM. 2017. Purification of DNA Damage-Dependent PARPs from E. coli for Structural and Biochemical Analysis. *PolyADP-Ribose Polym*, Methods in Molecular Biology 431–444. doi:10.1007/978-1-4939-6993-7_27

Lehmann LC, Bacic L, Hewitt G, Brackmann K, Sabantsev A, Gaullier G, Pytharopoulou S, Degliesposti G, Okkenhaug H, Tan S, Costa A, Skehel JM, Boulton SJ, Deindl S. 2020. Mechanistic Insights into Regulation of the ALC1 Remodeler by the Nucleosome Acidic Patch. *Cell Rep* **33**. doi:10.1016/j.celrep.2020.108529

Lehmann LC, Hewitt G, Aibara S, Leitner A, Marklund E, Maslen SL, Maturi V, Chen Y, Spoel D van der, Skehel JM, Moustakas A, Boulton SJ, Deindl S. 2017. Mechanistic Insights into Autoinhibition of the Oncogenic Chromatin Remodeler ALC1. *Mol Cell* **68**:847-859.e7. doi:10.1016/j.molcel.2017.10.017

Li Meijing, Xia X, Tian Y, Jia Q, Liu X, Lu Y, Li Ming, Li X, Chen Z. 2019. Mechanism of DNA translocation underlying chromatin remodelling by Snf2. *Nature* 1. doi:10.1038/s41586-019-1029-2

Liebschner D, Afonine PV, Baker ML, Bunkóczi G, Chen VB, Croll TI, Hintze B, Hung L-W, Jain S, McCoy AJ, Moriarty NW, Oeffner RD, Poon BK, Prisant MG, Read RJ, Richardson JS, Richardson DC, Sammito MD, Sobolev OV, Stockwell DH, Terwilliger TC, Urzhumtsev AG, Videau LL, Williams CJ, Adams PD. 2019. Macromolecular structure determination using X-rays, neutrons and electrons: recent developments in Phenix. *Acta Crystallogr Sect Struct Biol* **75**:861–877. doi:10.1107/S2059798319011471

Liu C, Vyas A, Kassab MA, Singh AK, Yu X. 2017. The role of poly ADP-ribosylation in the first wave of DNA damage response. *Nucleic Acids Res* **45**:8129–8141. doi:10.1093/nar/gkx565

Liu X, Li M, Xia X, Li X, Chen Z. 2017. Mechanism of chromatin remodelling revealed by the Snf2-nucleosome structure. *Nature* **544**:440–445. doi:10.1038/nature22036

Lowary PT, Widom J. 1998. New DNA sequence rules for high affinity binding to histone octamer and sequence-directed nucleosome positioning. *J Mol Biol* **276**:19–42. doi:10.1006/jmbi.1997.1494

Lu X, Simon MD, Chodaparambil JV, Hansen JC, Shokat KM, Luger K. 2008. The effect of H3K79 dimethylation and H4K20 trimethylation on nucleosome and chromatin structure. *Nat Struct Mol Biol* **15**:1122–1124. doi:10.1038/nsmb.1489

Ludwigsen J, Pfennig S, Singh AK, Schindler C, Harrer N, Forné I, Zacharias M, Mueller-Planitz F. 2017. Concerted regulation of ISWI by an autoinhibitory domain and the H4 N-terminal tail. *eLife* **6**:e21477. doi:10.7554/eLife.21477

Markert JW, Zhou K, Luger K. 2021. Structure and function of the chromatin remodeler SMARCAD1 with its nucleosome substrate. *bioRxiv* 2021.04.14.439859. doi:10.1101/2021.04.14.439859

Morgan MT, Haj-Yahya M, Ringel AE, Bandi P, Brik A, Wolberger C. 2016. Structural basis for histone H2B deubiquitination by the SAGA DUB module. *Science* **351**:725–728. doi:10.1126/science.aac5681

Muthurajan U, Mattiroli F, Bergeron S, Zhou K, Gu Y, Chakravarthy S, Dyer P, Irving T, Luger K. 2016. In Vitro Chromatin Assembly: Strategies and Quality ControlMethods in Enzymology. Elsevier. pp. 3–41.

Nakane T, Kimanius D, Lindahl E, Scheres SH. 2018. Characterisation of molecular motions in cryo-EM single-particle data by multi-body refinement in RELION. *eLife* **7**:e36861. doi:10.7554/eLife.36861

Nørby JG. 1988. [11] Coupled assay of Na+,K+-ATPase activityMethods in Enzymology, Biomembranes Part P: ATP-Driven Pumps and Related Transport: The Na,K-Pump. Academic Press. pp. 116–119. doi:10.1016/0076-6879(88)56014-7

Obaji E, Haikarainen T, Lehtiö L. 2018. Structural basis for DNA break recognition by ARTD2/PARP2. *Nucleic Acids Res* **46**:12154–12165. doi:10.1093/nar/gky927

Patel AB, Moore CM, Greber BJ, Luo J, Zukin SA, Ranish J, Nogales E. 2019. Architecture of the chromatin remodeler RSC and insights into its nucleosome engagement. *eLife* **8**:e54449. doi:10.7554/eLife.54449

Pettersen EF, Goddard TD, Huang CC, Meng EC, Couch GS, Croll TI, Morris JH, Ferrin TE. 2021. UCSF ChimeraX: Structure visualization for researchers, educators, and developers. *Protein Sci* **30**:70–82. doi:https://doi.org/10.1002/pro.3943

Punjani A, Fleet DJ. 2021. 3D Variability Analysis: Resolving continuous flexibility and discrete heterogeneity from single particle cryo-EM. *J Struct Biol* 107702. doi:10.1016/j.jsb.2021.107702

Punjani A, Rubinstein JL, Fleet DJ, Brubaker MA. 2017. cryoSPARC: algorithms for rapid unsupervised cryo-EM structure determination. *Nat Methods* **14**:290–296. doi:10.1038/nmeth.4169

Punjani A, Zhang H, Fleet DJ. 2020. Non-uniform refinement: adaptive regularization improves single-particle cryo-EM reconstruction. *Nat Methods* **17**:1214–1221. doi:10.1038/s41592-020-00990-8

Racki LR, Naber N, Pate E, Leonard JD, Cooke R, Narlikar GJ. 2014. The Histone H4 Tail Regulates the Conformation of the ATP-Binding Pocket in the SNF2h Chromatin Remodeling Enzyme. *J Mol Biol* **426**:2034–2044. doi:10.1016/j.jmb.2014.02.021

Reed MC, Lieb A, Nijhout HF. 2010. The biological significance of substrate inhibition: A mechanism with diverse functions. *BioEssays* **32**:422–429. doi:https://doi.org/10.1002/bies.200900167

Rohou A, Grigorieff N. 2015. CTFFIND4: Fast and accurate defocus estimation from electron micrographs. *J Struct Biol*, Recent Advances in Detector Technologies and Applications for Molecular TEM **192**:216–221. doi:10.1016/j.jsb.2015.08.008

Sellou H, Lebeaupin T, Chapuis C, Smith R, Hegele A, Singh HR, Kozlowski M, Bultmann S, Ladurner AG, Timinszky G, Huet S. 2016. The poly(ADP-ribose)-dependent chromatin remodeler Alc1 induces local chromatin relaxation upon DNA damage. *Mol Biol Cell* **27**:3791–3799. doi:10.1091/mbc.E16-05-0269

Singh HR, Nardozza AP, Möller IR, Knobloch G, Kistemaker HAV, Hassler M, Harrer N, Blessing C, Eustermann S, Kotthoff C, Huet S, Mueller-Planitz F, Filippov DV, Timinszky G, Rand KD, Ladurner AG. 2017. A Poly-ADP-Ribose Trigger Releases the Auto-Inhibition of a Chromatin Remodeling Oncogene. *Mol Cell* **68**:860-871.e7. doi:10.1016/j.molcel.2017.11.019

Sundaramoorthy R, Hughes AL, El-Mkami H, Norman DG, Ferreira H, Owen-Hughes T. 2018. Structure of the chromatin remodelling enzyme Chd1 bound to a ubiquitinylated nucleosome. *eLife* **7**. doi:10.7554/eLife.35720

Sundaramoorthy R, Hughes AL, Singh V, Wiechens N, Ryan DP, El-Mkami H, Petoukhov M, Svergun DI, Treutlein B, Quack S, Fischer M, Michaelis J, Böttcher B, Norman DG, Owen-Hughes T. 2017. Structural reorganization of the chromatin remodeling enzyme Chd1 upon engagement with nucleosomes. *eLife* **6**:e22510. doi:10.7554/eLife.22510

Valencia-Sánchez MI, De Ioannes P, Wang M, Vasilyev N, Chen R, Nudler E, Armache J-P, Armache K-J. 2019. Structural Basis of Dot1L Stimulation by Histone H2B Lysine 120 Ubiquitination. *Mol Cell*. doi:10.1016/j.molcel.2019.03.029

Valencia-Sánchez MI, Ioannes PD, Wang M, Truong DM, Lee R, Armache J-P, Boeke JD, Armache K-J. 2021. Regulation of the Dot1 histone H3K79 methyltransferase by histone H4K16 acetylation. *Science* **371**. doi:10.1126/science.abc6663

Vasudevan D, Chua EYD, Davey CA. 2010. Crystal Structures of Nucleosome Core Particles Containing the '601' Strong Positioning Sequence. *J Mol Biol* **403**:1–10. doi:10.1016/j.jmb.2010.08.039

Verma P, Zhou Y, Cao Z, Deraska PV, Deb M, Arai E, Li W, Shao Y, Puentes L, Li Y, Patankar S, Mach RH, Faryabi RB, Shi J, Greenberg RA. 2021. ALC1 links chromatin accessibility to PARP inhibitor response in homologous recombination-deficient cells. *Nat Cell Biol* 1–12. doi:10.1038/s41556-020-00624-3

Wagner FR, Dienemann C, Wang H, Stützer A, Tegunov D, Urlaub H, Cramer P. 2020. Structure of SWI/SNF chromatin remodeller RSC bound to a nucleosome. *Nature* 1–4. doi:10.1038/s41586-020-2088-0

Wang H, Dienemann C, Stützer A, Urlaub H, Cheung ACM, Cramer P. 2020a. Structure of the transcription coactivator SAGA. *Nature* **577**:717–720. doi:10.1038/s41586-020-1933-5

Wang H, Farnung L, Dienemann C, Cramer P. 2020b. Structure of H3K36-methylated nucleosome–PWWP complex reveals multivalent cross-gyre binding. *Nat Struct Mol Biol* **27**:8–13. doi:10.1038/s41594-019-0345-4

Waterhouse A, Bertoni M, Bienert S, Studer G, Tauriello G, Gumienny R, Heer FT, de Beer TAP, Rempfer C, Bordoli L, Lepore R, Schwede T. 2018. SWISS-MODEL: homology modelling of protein structures and complexes. *Nucleic Acids Res* **46**:W296–W303. doi:10.1093/nar/gky427

Willhoft O, Ghoneim M, Lin C-L, Chua EYD, Wilkinson M, Chaban Y, Ayala R, McCormack EA, Ocloo L, Rueda DS, Wigley DB. 2018. Structure and dynamics of the yeast SWR1-nucleosome complex. *Science* **362**:eaat7716. doi:10.1126/science.aat7716

Wilson MD, Benlekbir S, Fradet-Turcotte A, Sherker A, Julien J-P, McEwan A, Noordermeer SM, Sicheri F, Rubinstein JL, Durocher D. 2016. The structural basis of modified nucleosome recognition by 53BP1. *Nature* **536**:100–103. doi:10.1038/nature18951

Worden EJ, Hoffmann NA, Hicks CW, Wolberger C. 2019. Mechanism of Cross-talk between H2B Ubiquitination and H3 Methylation by Dot1L. *Cell*. doi:10.1016/j.cell.2019.02.002

Worden EJ, Zhang X, Wolberger C. 2020. Structural basis for COMPASS recognition of an H2B-ubiquitinated nucleosome. *eLife* **9**:e53199. doi:10.7554/eLife.53199

Xue H, Yao T, Cao M, Zhu G, Li Y, Yuan G, Chen Y, Lei M, Huang J. 2019. Structural basis of nucleosome recognition and modification by MLL methyltransferases. *Nature* 1–6. doi:10.1038/s41586-019-1528-1

Yan L, Wu H, Li X, Gao N, Chen Z. 2019. Structures of the ISWI–nucleosome complex reveal a conserved mechanism of chromatin remodeling. *Nat Struct Mol Biol* 1. doi:10.1038/s41594-019-0199-9

Yang JG, Madrid TS, Sevastopoulos E, Narlikar GJ. 2006. The chromatin-remodeling enzyme ACF is an ATP-dependent DNA length sensor that regulates nucleosome spacing. *Nat Struct Mol Biol* **13**:1078–1083. doi:10.1038/nsmb1170

Yao T, Jing W, Hu Z, Tan M, Cao M, Wang Q, Li Y, Yuan G, Lei M, Huang J. 2019. Structural basis of the crosstalk between histone H2B monoubiquitination and H3

lysine 79 methylation on nucleosome. *Cell Res* **29**:330. doi:10.1038/s41422-019-0146-7

Ye Y, Wu H, Chen K, Clapier CR, Verma N, Zhang W, Deng H, Cairns BR, Gao N, Chen Z. 2019. Structure of the RSC complex bound to the nucleosome. *Science*. doi:10.1126/science.aay0033

Zheng SQ, Palovcak E, Armache J-P, Verba KA, Cheng Y, Agard DA. 2017. MotionCor2: anisotropic correction of beam-induced motion for improved cryo-electron microscopy. *Nat Methods* **14**:331. doi:10.1038/nmeth.4193

Zhong ED, Bepler T, Berger B, Davis JH. 2021. CryoDRGN: reconstruction of heterogeneous cryo-EM structures using neural networks. *Nat Methods* 1–10. doi:10.1038/s41592-020-01049-4

Zivanov J, Nakane T, Forsberg BO, Kimanius D, Hagen WJ, Lindahl E, Scheres SH. 2018. New tools for automated high-resolution cryo-EM structure determination in RELION-3. *eLife* **7**:e42166. doi:10.7554/eLife.42166

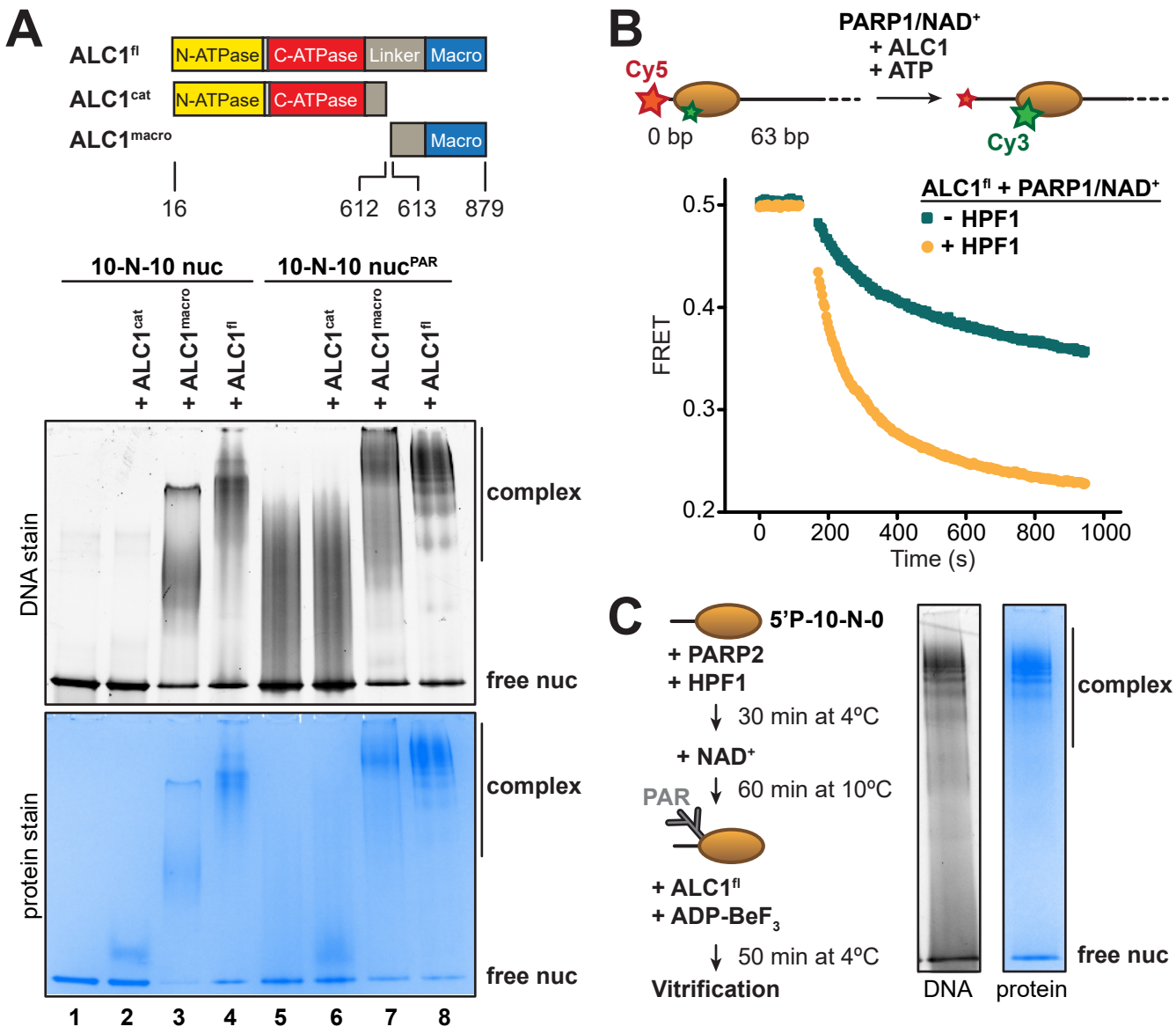

Figure 1, Bacic *et al.*

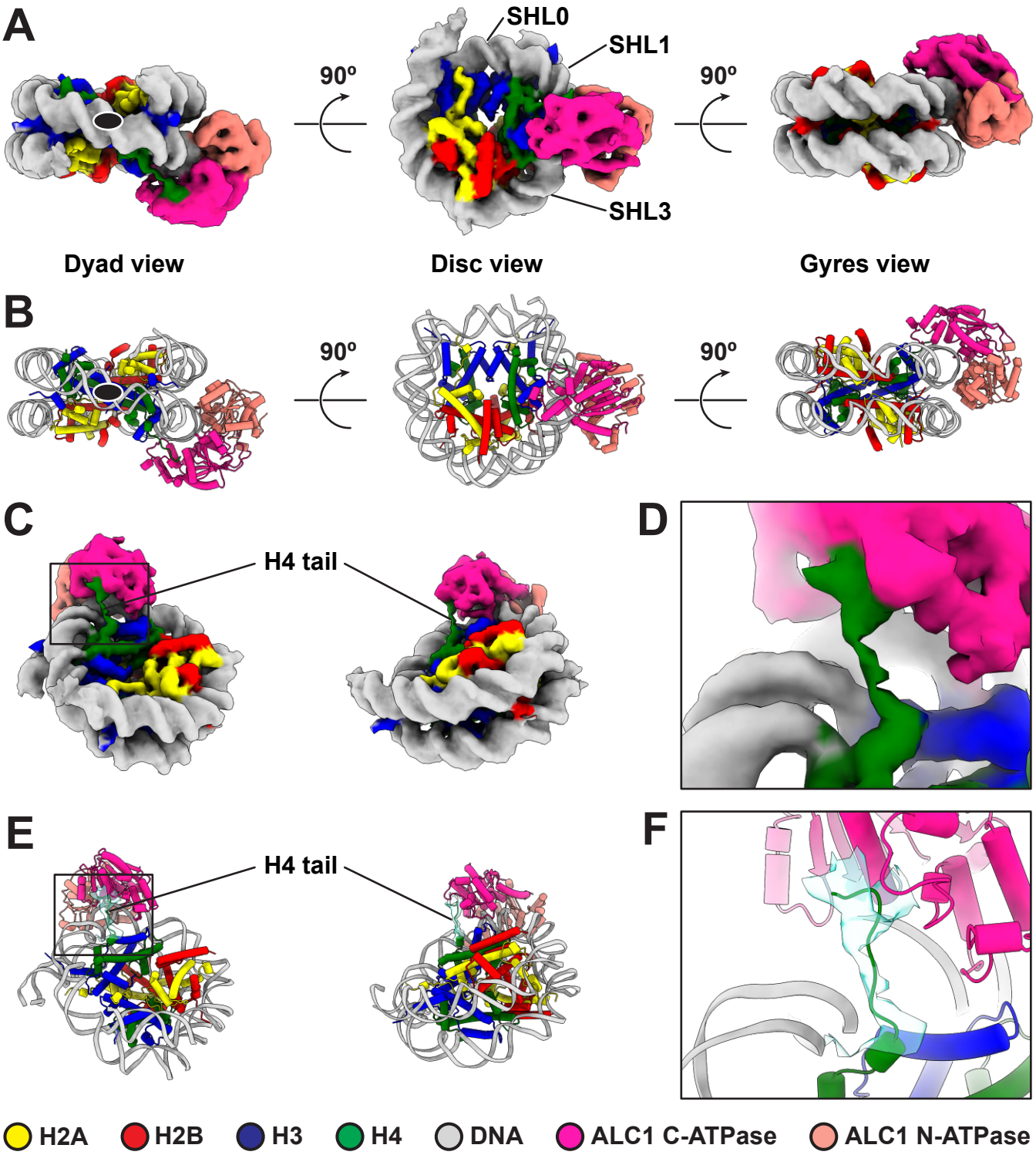

Figure 2, Bacic *et al*.

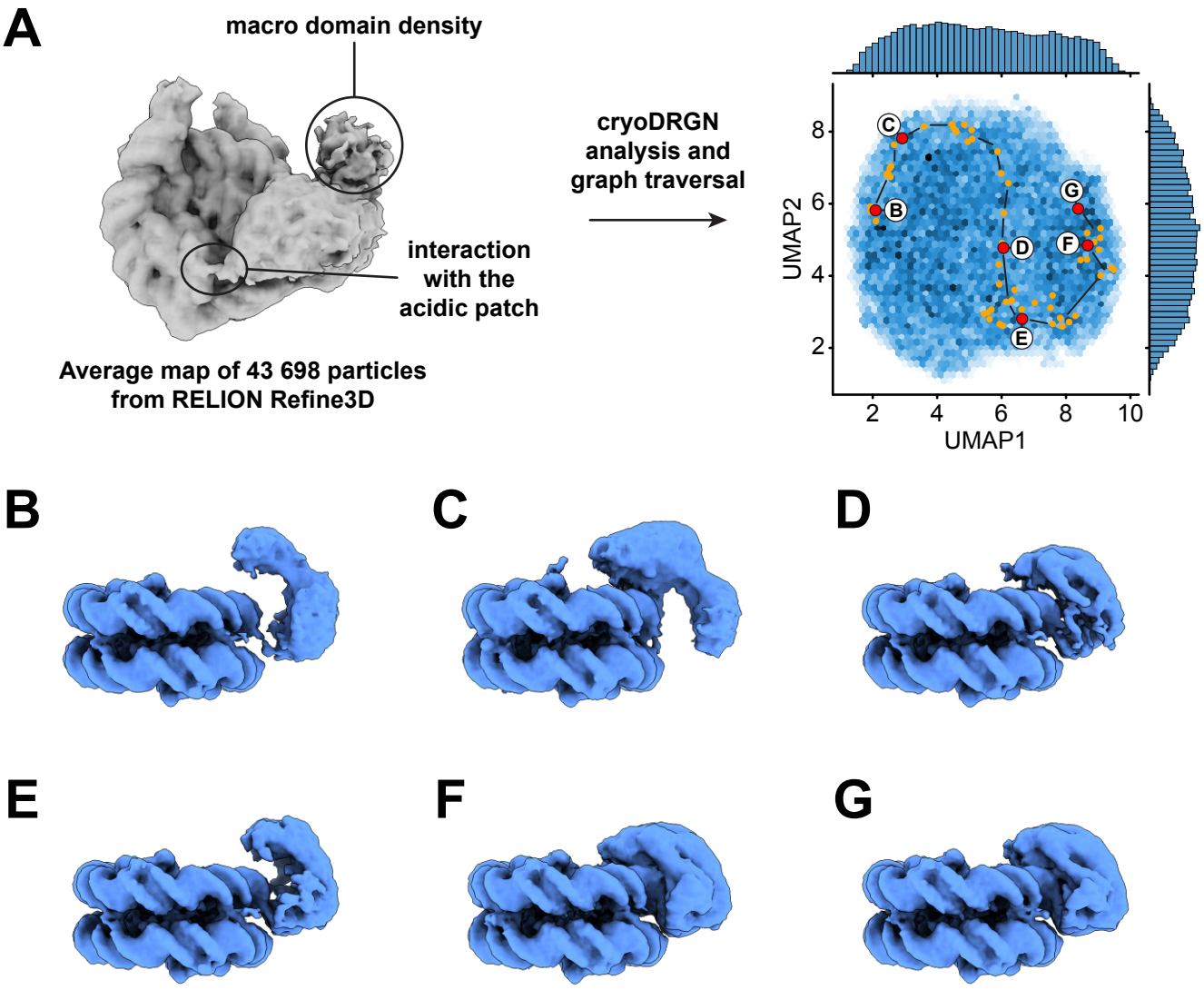

Figure 3, Bacic *et al*.

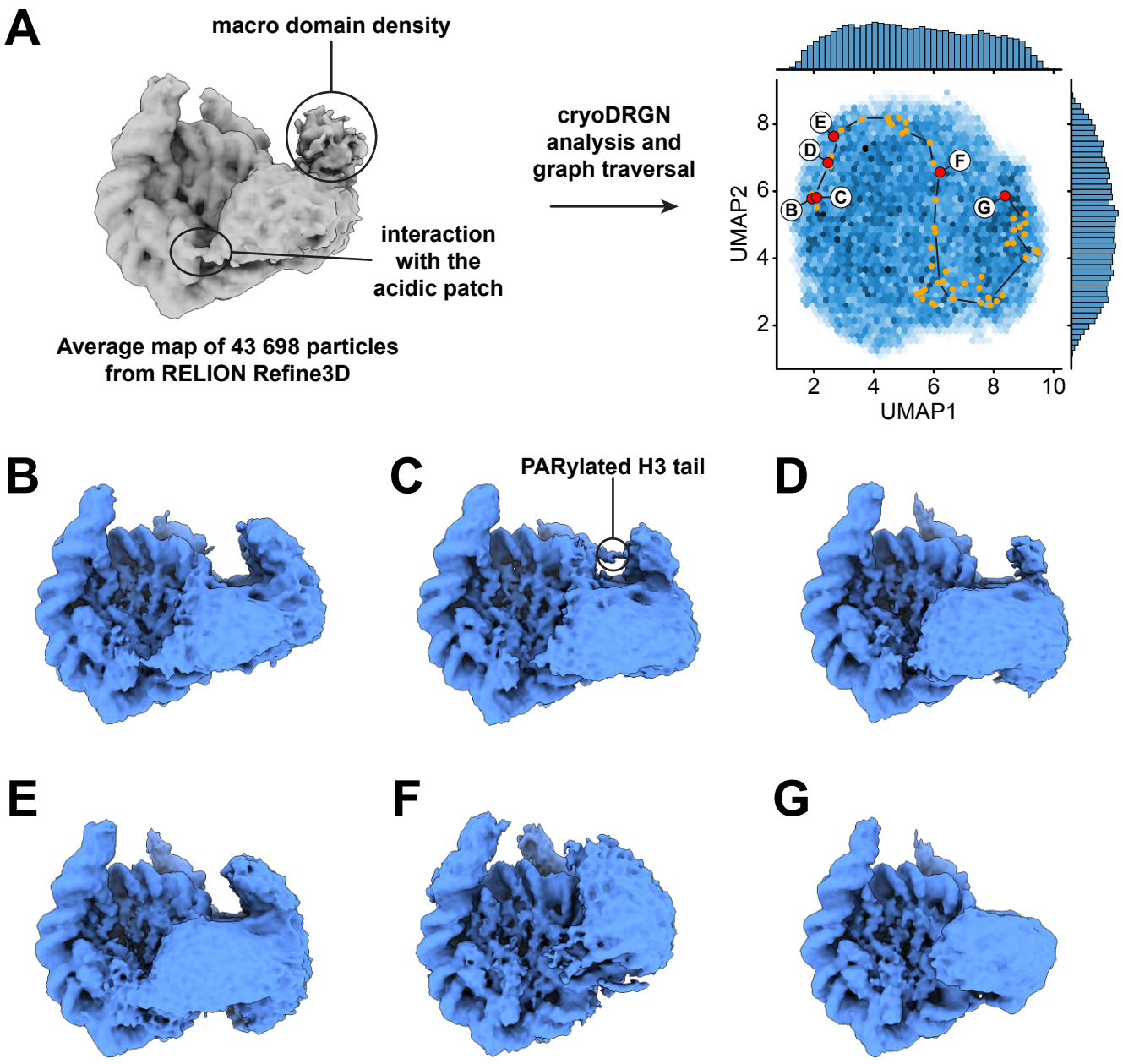

Figure 4, Bacic *et al*.

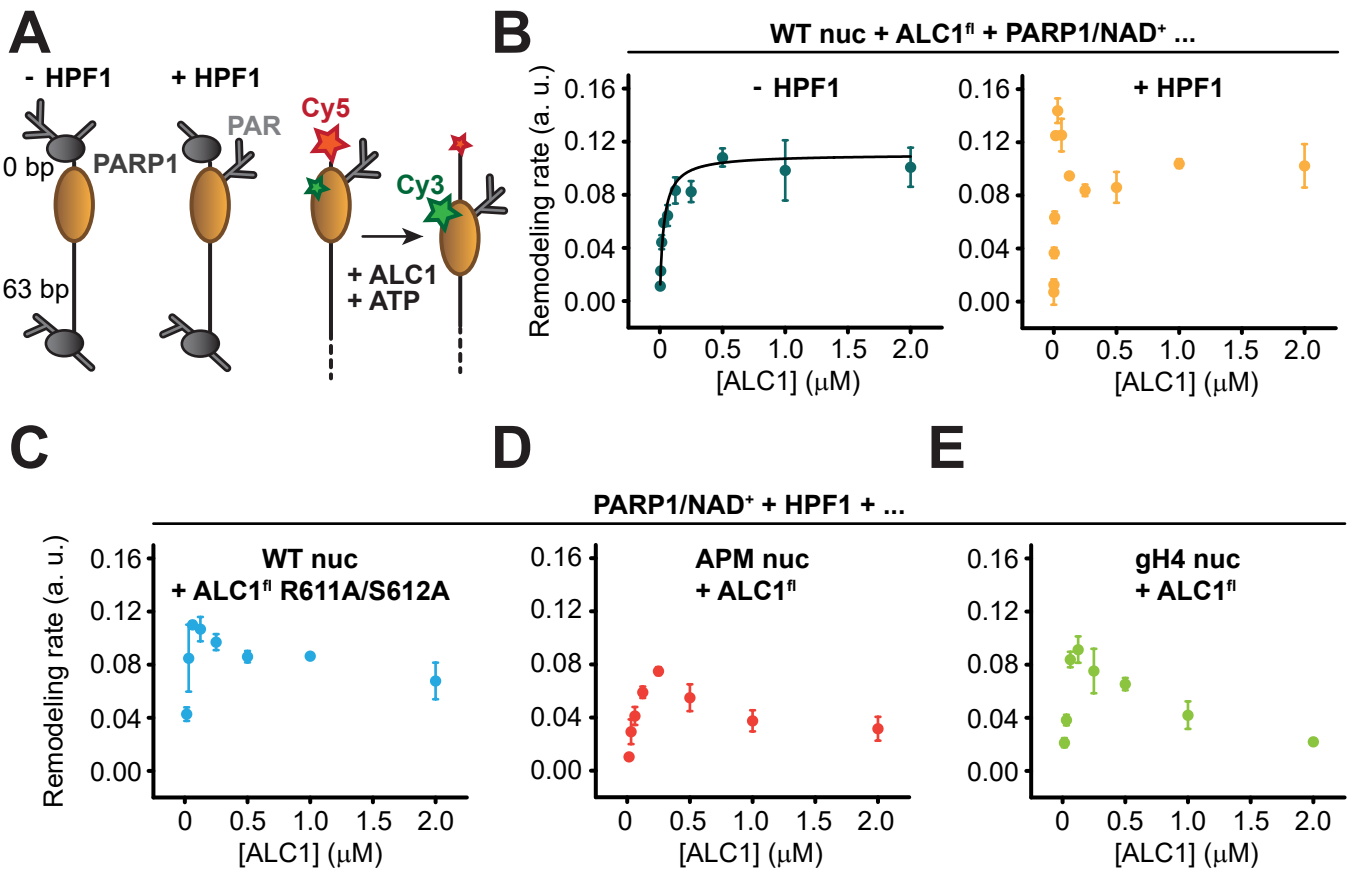

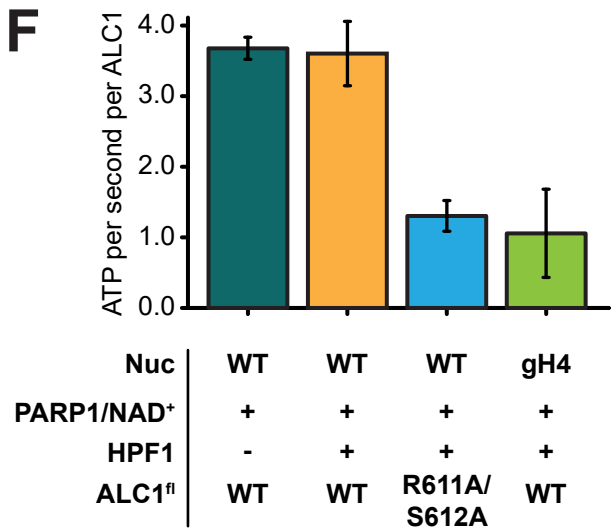

Figure 5, Bacic *et al*.

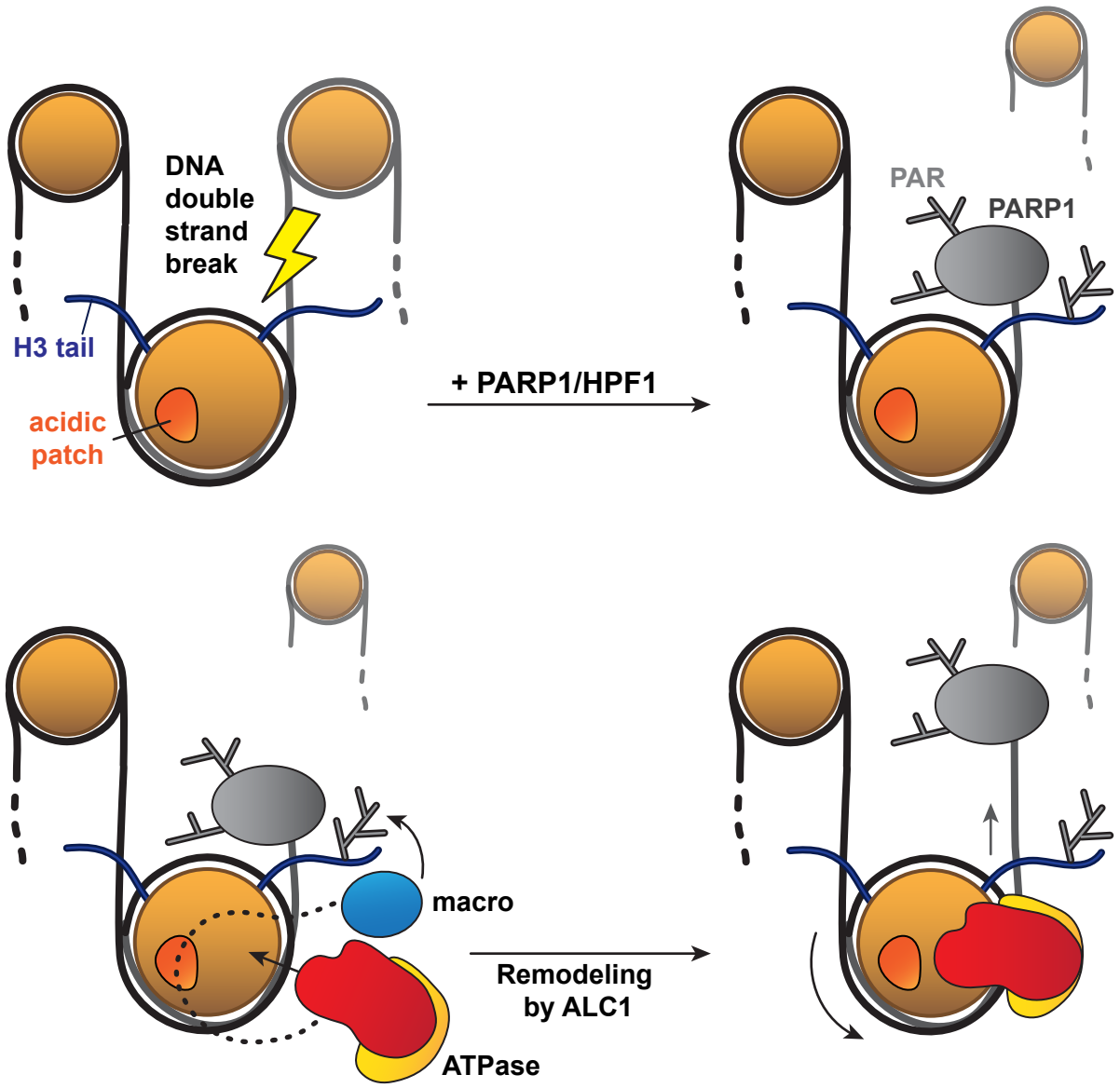

Figure 6, Bacic *et al*.

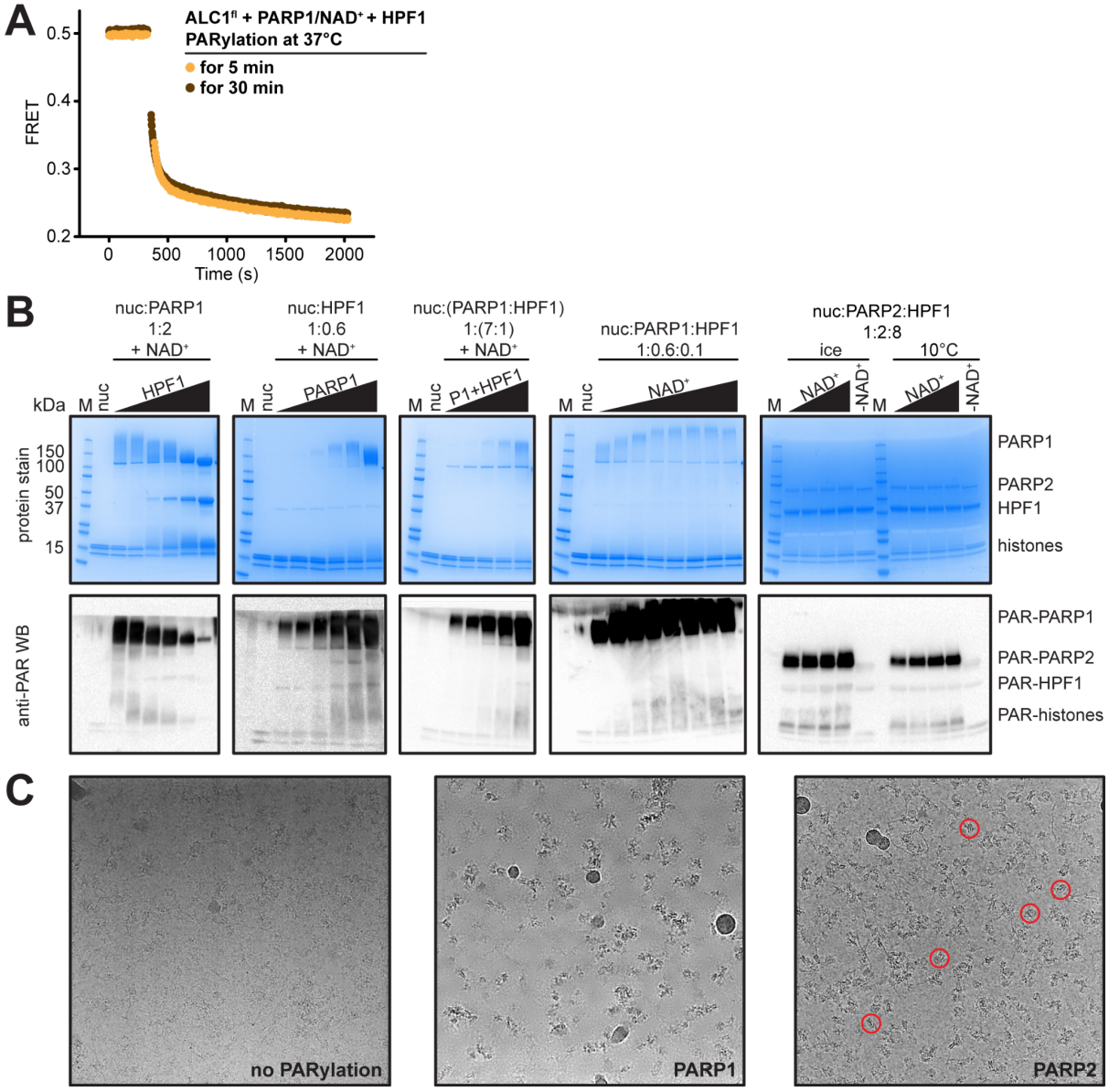

Figure S1. Related to Figure 1. Identification of an ALC1 - PARylated nucleosome complex suitable for cryo-EM.

(**A**) Nucleosome sliding assays with 5 minutes (orange) or 30 minutes (brown) incubation time of the PARylation reaction prior to the initiation of the sliding reaction. Superimposition of the sliding curves indicates that the PARylated nucleosome substrate is functionally identical between the two reactions, and therefore that 5 minutes of incubation is enough for the PARylation reaction to exhaust the limiting amount of NAD^+ provided.

(**B**) SDS-PAGE and Western blot analysis of different PARylation conditions of nucleosomes by PARP1/HPF1 or PARP2/HPF1.

(**C**) Screening micrographs of complexes prepared with ALC1 and nucleosomes either unmodified (left), PARylated by PARP1 and HPF1 (middle), or PARylated by PARP2 and HPF1 (right).

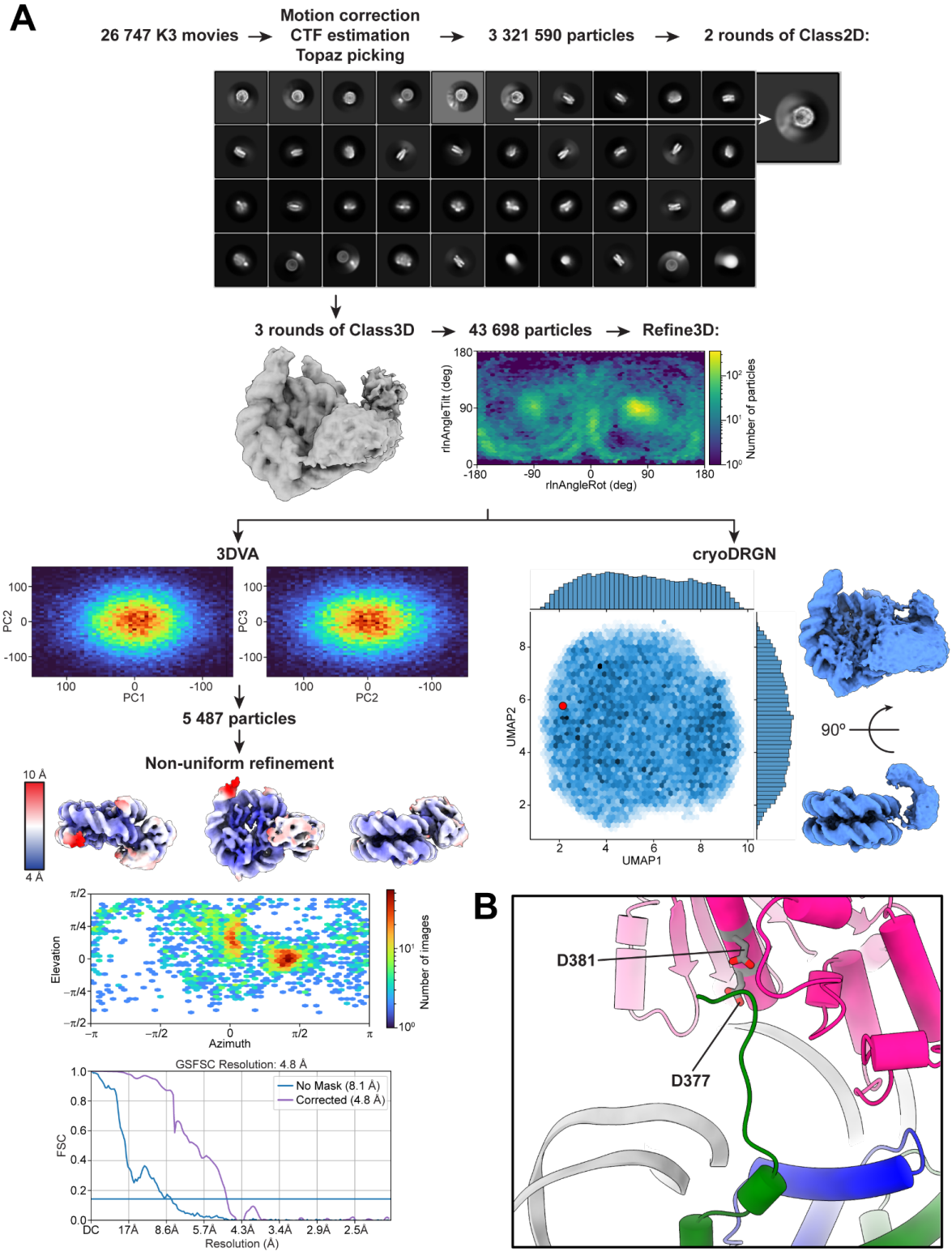

Figure S2. Related to Figure 2. Overview of cryo-EM data processing and refinement.

(**A**) Overview of cryo-EM data processing and analysis.

(**B**) Close-up view of the structure of the complex between a PARylated nucleosome and ALC1 in the tightly bound state, showing the H4 tail interacting with the C-terminal ATPase domain of ALC1. The same part of the complex is shown as in Figure 2F, with the two residues from ALC1, D377 and D381, shown as grey sticks.

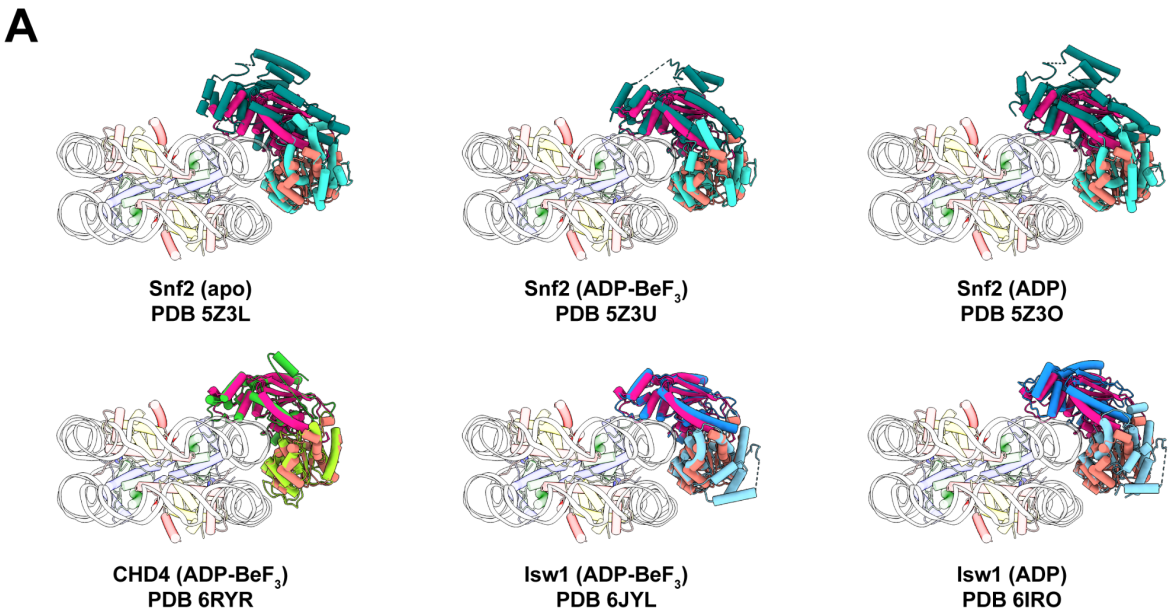

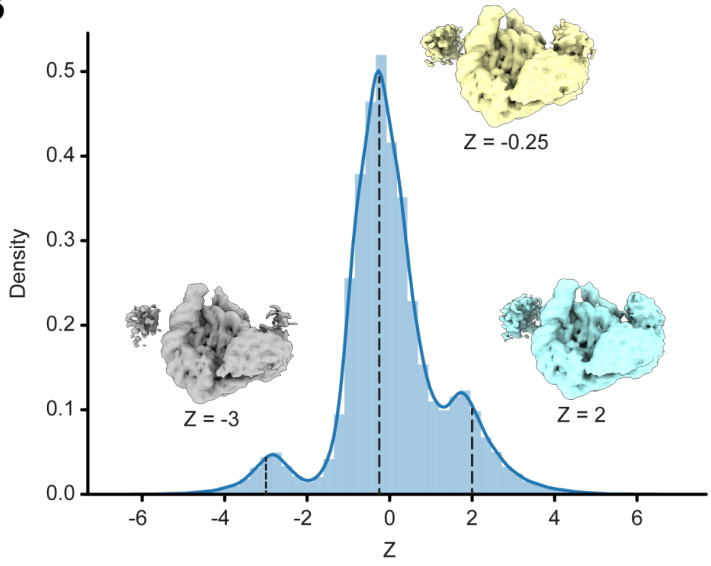

Figure S3. Related to Figure 3. Dynamics of the ATPase domain of ALC1.

(**A**) Superimposition of previous structures of remodeler-nucleosome complexes to our structure of the ALC1-nucleosome complex. ALC1 is colored in two shades of pink as in Figure 2. For clarity, only the ATPase motor is shown for structures also containing other domains.

(**B**) Distribution of Z values from a 1-dimensional latent variable training run of cryoDRGN. Maps generated by evaluating the decoder at Z values of the distribution's peaks are shown.

A

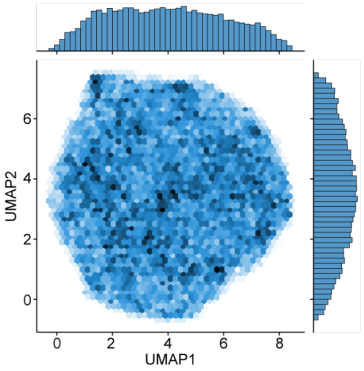

D = 128
Apix = 3.36
256x3
|z| = 8
Replicate 1

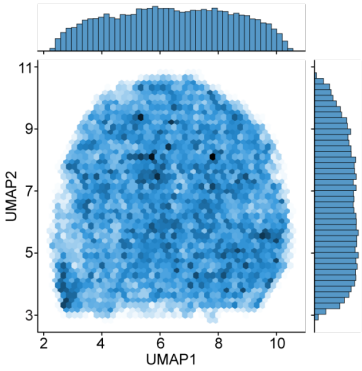

D = 128
Apix = 3.36
256x3
|z| = 8
Replicate 2

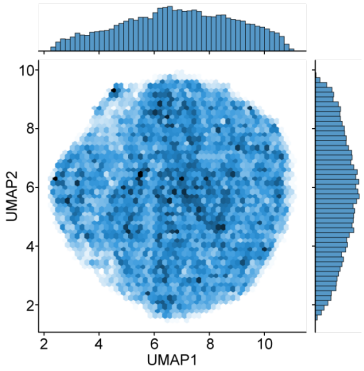

D = 128
Apix = 3.36
256x3
|z| = 8
Replicate 3

B

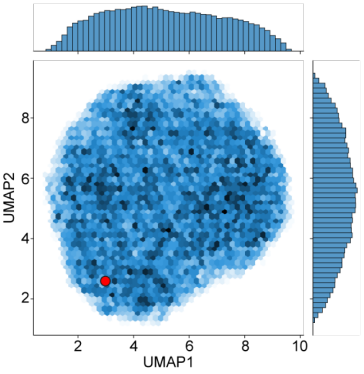

D = 128
Apix = 1.68
256x3
|z| = 8
Higher res. 1

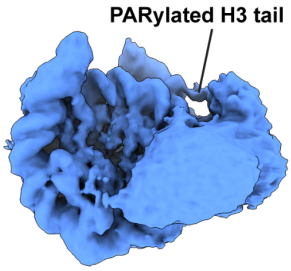

C

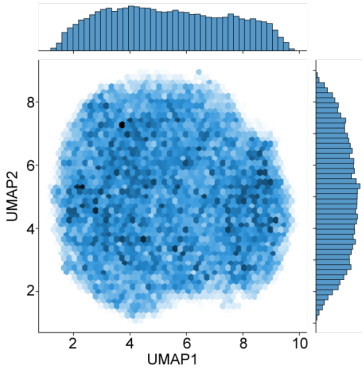

D = 128
Apix = 1.68
512x3
|z| = 8
Higher res. 2
(Same as in Figures 3 and 4)

Figure S4. Related to Figure 4. Analysis of heterogeneity in the cryo-EM dataset.

(**A**) UMAP visualizations of the latent variable distributions from three replicate training runs of cryoDRGN with independent initializations, and with the indicated image size, pixel size, network architecture and dimensionality of the latent variable.

(**B**) UMAP visualization of the latent variable distribution from a replicate training run of cryoDRGN with independent initialization, and with the indicated image size, pixel size, network architecture and dimensionality of the latent variable. The map displayed on the right was produced by evaluating the decoder at the Z values indicated by the red dot in the UMAP distribution.

(**C**) UMAP visualization of the latent variable distribution of the training run of cryoDRGN shown in Figures 3 and 4, with the indicated image size, pixel size, network architecture and dimensionality of the latent variable.

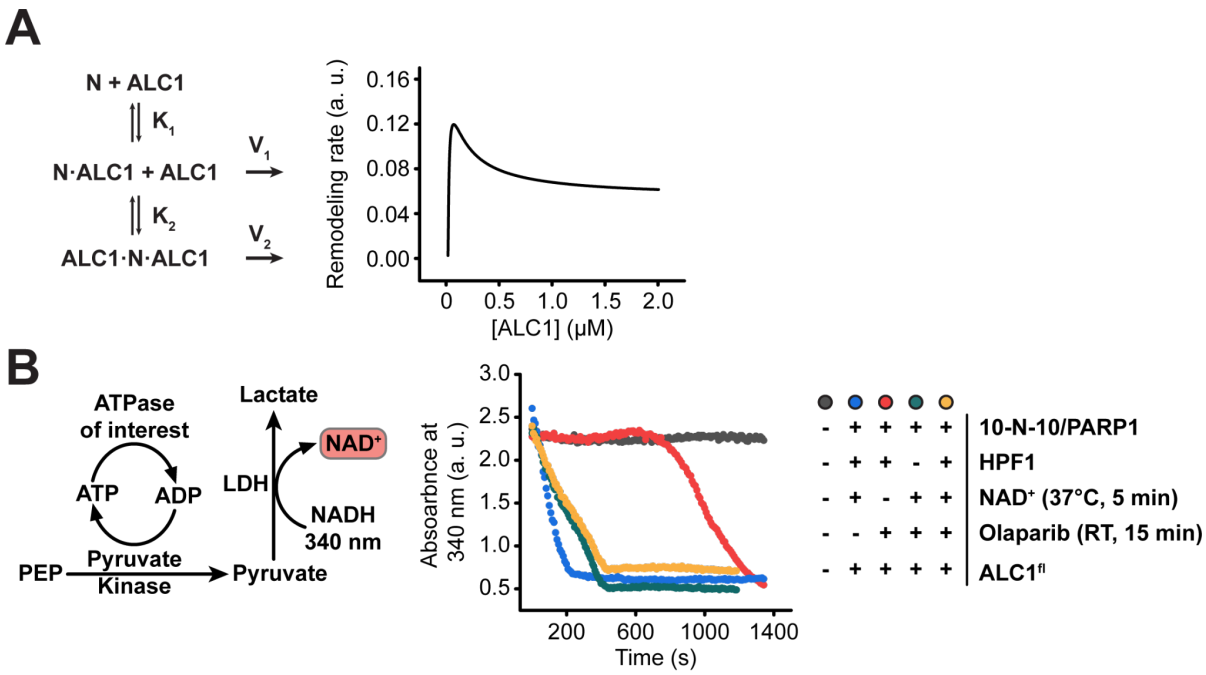

Figure S5. Related to Figure 5. ALC1 activity in nucleosome sliding and ATPase assays.

(**A**) A hypothetical reaction diagram (left) and a resulting saturation curve (right) for ALC1-catalyzed nucleosome sliding, where ALC1 first binds to the PARylated side of the nucleosome with a high affinity (K1), which results in fast unopposed sliding towards the longer linker (V1). ALC1 then binds to the other side of the nucleosome, which opposes sliding towards the longer linker and results in slower remodeling rate (V2). See Methods section for further details.

(**B**) Left: schematic of the ATPase assay used in this study. Right: Raw data curves for control ATPase assays. The assay produces NAD^+, which is the substrate of PARP1. We therefore include the PARP inhibitor Olaparib in our ATPase assays, to avoid further PARylation during the assay. See Methods section for a more detailed explanation.

Data collection and processing		
Acceleration voltage (kV)	300	
Spherical aberration (mm)	2.7	
Amplitude contrast (fraction)	0.1	
Image pixel size (Å/pixel)	0.84	
Electron exposure per frame ($e^-/Å^2$)	1.125	
Number of movie frames	40	
Total electron exposure ($e^-/Å^2$)	45	
Nominal defocus range (μm)	-1.0 to -2.5	
Number of movies collected	26 747	
Number of picked particles	3 321 590	
Particles used for reconstruction	5 487 (single map)	43 698 (cryoDRGN analysis)
Map symmetry imposed	C1	
Map sharpening B-factor ($Å^2$)	128.2	NA
Global resolution at 0.143 FSC (Å)	4.8	
Local resolution range (Å)	4-20	
Model building and refinement		
Initial models used (PDB codes)	Nucleosome (6RYR) Template for homology modeling of ALC1 ATPase (6JYL)	NA
Number of atoms (hydrogens)	29 161 (13 383)	
Number of protein residues	1 214	
Number of DNA residues	298	
Bond length RMSD (Å)	0.004	
Bond angles RMSD (°)	0.760	
MolProbity score	1.74	
Clash score	6.69	
Ramachandran outliers/allowed/favored (%)	0.25 / 3.68 / 96.07	
Rotamer outliers (%)	1.36	

Cβ outliers (%)	0.00	
CαBLAM outliers (%)	2.72	
Model to map CC (mask/box/peaks/volume)	0.77 / 0.84 / 0.71 / 0.77	

Table S1. Related to Figure 2. Cryo-EM data collection and refinement statistics.

Number of particles	Image size (pixels)	Pixel size (Å/pixel)	Image size (Å)	Dimension of Z	Network architecture	Number of epochs	Goal
43 698	128	3.36	430	1	256x3	50	Detection of junk
43 698	128	3.36	430	8	256x3	50	Evaluation (rep. 1)
43 698	128	3.36	430	8	256x3	50	Evaluation (rep. 2)
43 698	128	3.36	430	8	256x3	50	Evaluation (rep. 3)
43 698	128	1.68	215	8	256x3	50	Higher res. 1
43 698	128	1.68	215	8	512x3	50	Higher res. 2

Table S2. Related to Figure 3. Settings of cryoDRGN training runs.